Spin squeezed states and wobbling motion in a collective Hamiltonian

Q. B. Chen [1,*] and S. Frauendorf [2,†]
[1]*Department of Physics, East China Normal University, Shanghai 200241, China*
[2]*Physics Department, University of Notre Dame, Notre Dame, Indiana 46556, USA*

(Received 27 December 2023; accepted 12 March 2024; published 1 April 2024)

A semiclassical approach combined with adiabatic approximation is applied to the particle+triaxial rotor (PTR) model in order to derive the collective potential and mass parameters of a collective Hamiltonian (CH) that depends only on the total angular momentum for the wobbling motion. The CH approximates very well the energies and $E2$ transition probabilities associated with the lowest wobbling states in both even-even and odd-mass systems. The spin squeezed state (SSS) representation with the character of a wave function in orientation angle of the total angular momentum is introduced to illustrate on the structure of the states. The probability distribution for the lowest states of the PTR and the CH agree well. This demonstrates that the method can be used to incorporate collective wobbling into the microscopic tilted axis cranking approach. A classification scheme for the wobbling mode based on the SSS states is discussed.

DOI: 10.1103/PhysRevC.109.044304

I. INTRODUCTION

Nuclear wobbling motion, originally proposed by Bohr and Mottelson [1], is a unique phenomenon observed in triaxially deformed rotating nuclei. This motion involves the nucleus rotating around the principal axis with the largest moment of inertia, which then executes harmonic oscillations about the space-fixed angular momentum vector. The energy spectra associated with this motion produce a series of rotational $E2$ bands that correspond to different oscillation quanta (n). These bands are characterized by transitions with $\Delta I = 1$, which predominantly exhibit $E2$ character.

However, the existence of wobbling motion in even-even nuclei, where no intrinsic angular momentum is involved, remains unconfirmed experimentally. Wobbling bands have been observed in odd-mass nuclei, where the coupling between a triaxial rotor and a high-j particle or hole can give rise to two distinct wobbling modes [2]. These modes are referred to as longitudinal wobbling (LW) and transverse wobbling (TW), depending on whether the angular momentum of the high-j particle or hole is parallel or perpendicular to the principal axis with the largest moment of inertia. Consequently, the wobbling energy increases with spin for LW, while it decreases for TW [2]. In a subsequent work by Chen and Frauendorf [3], a more comprehensive classification of wobbling motion was introduced based on the topology of classical orbits visualized using corresponding spin coherent state (SCS) maps. These maps (also called as azimuthal plots in Refs. [4–6] when applied for the visualization of total angular momentum) provide probability distributions for the orientation of the angular momentum on the unit sphere projected onto the polar angle θ and azimuthal angle ϕ plane. According to this classification, LW corresponds to a revolution of the total angular momentum $\boldsymbol{J}$ around the axis with the largest moment of inertia, whereas TW corresponds to a revolution of $\boldsymbol{J}$ around an axis perpendicular to the axis with the largest moment of inertia. By employing these scientific classifications and models, one has gained a deeper understanding of the wobbling motions exhibited by triaxial rotors coupled with high-j quasiparticles.

Currently, the experimental observations of wobbling bands are primarily reported in odd-proton nuclei. Notable examples include ^{161}Lu [7], ^{163}Lu [8,9], ^{165}Lu [10], ^{167}Lu [11], ^{167}Ta [12], and the most recent discovery in ^{151}Eu [13] in the $A \approx 160$ mass region, ^{135}Pr [14,15] and ^{133}La [16] in the $A \approx 130$ mass region, and ^{187}Au [17] and ^{183}Au [18] in the $A \approx 190$ mass region. Additionally, wobbling bands have been observed in odd-neutron nuclei such as ^{105}Pd [19], ^{127}Xe [20], and ^{133}Ba [21]. More recently, wobbling bands have also been pointed out in even-even nuclei with a two-quasiparticle configuration, specifically in ^{130}Ba [22–24] and ^{136}Nd [25,26]. It is important to acknowledge that certain proposed wobblers continue to be a topic of controversy [27–34]. Nevertheless, these experimental observations contribute to the scientific understanding of wobbling motion in various nuclear systems.

On the theoretical front, the wobbling motion was initially proposed within the framework of the triaxial rotor model (TRM) [1]. The TRM allows for an investigation of the angular momentum geometry associated with the wobbling motion in a triaxially deformed even-even nucleus [3,35,36]. Subsequent to the discovery of the first wobbling structure in the odd-proton nucleus ^{163}Lu [8], the particle-triaxial-rotor (PTR) model [2,3,6,23,37–43] and its approximate solutions [44–49] have been employed to describe the wobbling mode.

*Corresponding author: qbchen@phy.ecnu.edu.cn
†Corresponding author: sfrauend@nd.edu

In addition, various efforts have been made to extend the cranking model within the mean-field theory framework in order to study the wobbling motion. Due to the mean-field approximation, the cranking model only yields the yrast sequence for a given configuration. To describe wobbling excitations, it is necessary to go beyond the mean-field approximation. Currently, this has been achieved by incorporating quantum correlations through methods such as the random-phase approximation [50–56], the angular momentum projection method [24,25,57], and the collective Hamiltonian (CH) method [58,59]. Notably, the collective Hamiltonian framework has also achieved considerable success in describing chiral motion [60–62], which is also the fingerprint of the triaxial deformation. These theories offer means to incorporate quantum effects beyond the mean-field level in the study of wobbling motion.

The present paper further develops of the CH approximation for the PTR model. One reason is that the collective Hamiltonian provides an instructive perspective on the results of full the PTR calculations in terms of the familiar "potential + kinetic energy" paradigm. It provides another view on the physics of the coupled system that is complementary the SCS maps of the classical orbits on the surface of the angular momentum sphere, which we developed in Ref. [3]. Both approaches provide an extended classification of the collective mode into LW and TW, which is based on whether the total angular momentum revolves, respectively, the medium principal axis with the maximal moment of inertia or an axis perpendicular to it. This scheme extends the original LW-TW classification introduced in Ref. [2], which is based on whether the particle is aligned with the medium axis or an axis perpendicular to it, by taking into account the reorientation of the particle caused by the Coriolis force. In this way the transition with increasing angular momentum from TW to LW via a flip mode is correctly described.

The other motivation for the present study is that the construction of the CH from the adiabatic energy can be applied to the microscopic tilted axis cranking (TAC) calculations. Our future work will explore this avenue. The present study is a proof of principle. We demonstrate how derive a CH from the TAC-like adiabatic energy, which reproduces with good accuracy the first and second wobbling bands of the PTR model, which we can directly calculate.

Compared to earlier versions collective Hamiltonian approach in Refs. [58–62], the present paper proposes a novel approach in which both the collective potential and mass parameter of collective Hamiltonian are derived from the semiclassical adiabatic energy, and the total angular momentum retains its nature as a good quantum number.

Furthermore, to enable a comprehensive comparison between the wave functions derived using different models, this work will introduce the concept of spin squeezed states (SSS). Squeezed states, initially introduced in the domain of quantum optics [63], represent a generalization of coherent states [64]. In contrast to coherent states, which minimize the uncertainty product $\Delta x \Delta p$, squeezed states exhibit a smaller uncertainty in either Δx or Δp at the expense of a larger complementary width. The SSS states provide a valuable interpretation from a quantum mechanical perspective as they connect the discrete $\boldsymbol{J}$-space representation with the continuous coordinate ϕ's wave function. This approach allows for a deeper understanding of the wobbling motion within the context of the collective Hamiltonian framework, providing insights that go beyond the scope of traditional analysis.

II. THEORETICAL FRAMEWORK

A. Spin squeezed states

The Hilbert space of the quantal system with one degree of freedom and good absolute angular momentum j is spanned by the "k states" $|k\rangle$, which possess a projection $-j \leqslant k \leqslant j$ on the quantization 3-axis. The motion of the system is subject to the constraint imposed by the conservation of angular momentum, which restricts it to the sphere of constant angular momentum,

$$\boldsymbol{j}^2 = j_1^2 + j_2^2 + j_3^2 = j(j+1). \tag{1}$$

In the context of this quantal system, it is possible to identify the angular momentum projection operator $\hat{j}_3$ as the momentum operator $\hat{p}$, which represents the momentum along a particular direction. Consequently, the angle operator $\hat{\phi}$, responsible for determining the orientation of the angular momentum vector $\hat{\boldsymbol{j}}$ projection in the 1-2-plane, can be interpreted as the conjugate position operator $\hat{q}$. This interpretation allows us to establish a correspondence between the quantum mechanical operators and their classical counterparts. In particular, we find the following commutation relation

$$[\hat{p}, \hat{q}] = [\hat{j}_3, \hat{\phi}] = -i. \tag{2}$$

In the classical counterpart of the system, the quantities j_3 and ϕ correspond to the canonical variables p and q, respectively.

In the following, we introduce the SSS. The overcomplete, nonorthogonal set of SSS are expressed in terms of k states as

$$|\phi\rangle = \frac{1}{\sqrt{2j+1}} \sum_{k=-j}^{j} e^{i\phi k} |k\rangle = \mathscr{R}_3^\dagger(\phi)|\phi = 0\rangle, \tag{3}$$

which are generated by rotating the state $|\phi = 0\rangle$ state about the 3-axis within the range $-\pi \leqslant \phi \leqslant \pi$. Note that in the case of half-integer j, the spinor $|k\rangle$ obeys $\mathscr{R}_3^\dagger(2\pi)|k\rangle = -|k\rangle$, which implies $|\phi + 2\pi\rangle = -|\phi\rangle$. For this reason the explicit definition of the ϕ range is of importance. The SSS states are normalized but nonorthogonal,

$$|\langle\phi|\phi'\rangle| = \begin{cases} 1, & \text{if } \phi = \phi', \\ \left|\frac{\sin[(j+1/2)(\phi-\phi')]}{(2j+1)\sin[(\phi-\phi')/2]}\right|, & \text{if } \phi \neq \phi'. \end{cases} \tag{4}$$

The overlap $|\langle\phi_n|\phi'\rangle| \approx 0.64$ at $\phi' = (\phi_n + \phi_{n+1})/2$ and $= 0$ at $\phi' = \phi_{n+1}$.

The SSS set is massively overcomplete, because the dimension of the $\boldsymbol{j}$ space is $2j+1$, whereas the dimension of the SSS space is infinite. There are infinite many possible transformations from the SSS basis back to the k-basis. One obvious transformation is

$$|jk\rangle = \frac{\sqrt{2j+1}}{2\pi} \int_{-\pi}^{\pi} d\phi\, e^{-i\phi k} |\phi\rangle, \tag{5}$$

which corresponds to the resolution of the identity operator,

$$\hat{1} = \sum_k |jk\rangle\langle jk| = \frac{2j+1}{2\pi}\int_{-\pi}^{\pi} d\phi\, |\phi\rangle\langle\phi|. \tag{6}$$

The probability distribution of the SSS is given by

$$P(\phi)_\nu = \frac{1}{2\pi}\sum_{K,K'=-I}^{I} e^{-i(K-K')\phi}\rho^{(\nu)}_{KK'}, \tag{7}$$

where ϕ is the angle with the short axis in the short-medium axis plane. The $\rho^{(\nu)}_{KK'}$ is the density matrix or the reduced density matrix composed by the expansion coefficient of the eigenfunction on the basis [3]. In the framework of TRM and the collective Hamiltonian introduced subsequently in Sec. II B, the coefficients are denoted as $C^{(\nu)}_{IK}$, and $\rho^{(\nu)}_{KK'}$ is calculated by [3]

$$\rho^{(\nu)}_{KK'} = C^{(\nu)}_{IK} C^{(\nu)*}_{IK'}. \tag{8}$$

In the PTR model with the coefficients $C^{(\nu)}_{IKk}$ (with k here being the projection of the particle angular momentum on the quantizated 3-axis), $\rho^{(\nu)}_{KK'}$ is the reduced density matrix [3],

$$\rho^{(\nu)}_{KK'} = \sum_k C^{(\nu)}_{IKk} C^{(\nu)*}_{IK'k}, \tag{9}$$

which is constructed by averaging over the degrees of freedom k that are not of interest for the moment.

The SSS probability fulfills the normalization condition as

$$\int_{-\pi}^{\pi} P(\phi)_\nu\, d\phi = 1. \tag{10}$$

A complete orthogonal basis can be also spanned by the discrete "ϕ states" $|\phi_n\rangle$, which are the SSS taken at the discrete angles $\phi_n = \frac{2\pi(n-j)}{2j+1}$, $n = 0, \ldots, 2j$ [cf. Eq. (4)]. The deviation of these "angle states" from being eigenstates of $e^{i\hat{\phi}}$ is of the order $1/2j$. They are localized in ϕ around ϕ_n. The SSS interpolate between the discrete ϕ states, which provides the information about the phase relations between the discrete ϕ states.

Figure 1 illustrates the basis sets of k states, ϕ states, SSS, as well as SCS used in Ref. [3]. The set of k states is orthonormal and complete. The j_3 takes the sharp values k while ϕ is uniformly distributed over the circles of constant latitude, which is often illustrated in form of a precession cones. For the ϕ states, $\hat{\phi}$ is localized at the discrete values ϕ_n while j_3 is uniformly distributed over the semicircles of constant longitude, which can be imagined as a semicircular sheets. They represent the momentum and coordinate representations of the states in the $\boldsymbol{j}$ space. As mentioned above, the SSS states interpolate between the discrete ϕ states, facilitating the extraction of phase relations among these discrete states. The set of the SCS is generated by rotating the generating state $|j, k = j\rangle$ over the whole angular momentum sphere [3].

It is noted that the authors of Refs. [44–49] used the SCS with the original complex number parameters. The one-to-correspondence with the more intuitive parametrization in Fig. 1 is discussed in Ref. [65].

The notation squeezed states comes from quantum optics. They are a generalization of coherent states. For coherent states the uncertainty product $\Delta x \Delta p$ is minimized. For squeezed states either Δx or Δp is smaller than for the optimal coherent states (and the complementary width is larger). The SSS uncertainty $\Delta\phi \approx 3/(2j)$ [see Eq. (4)] is smaller than the SCS width of $1/\sqrt{2j}$ because k has a large width of $2j+1$.

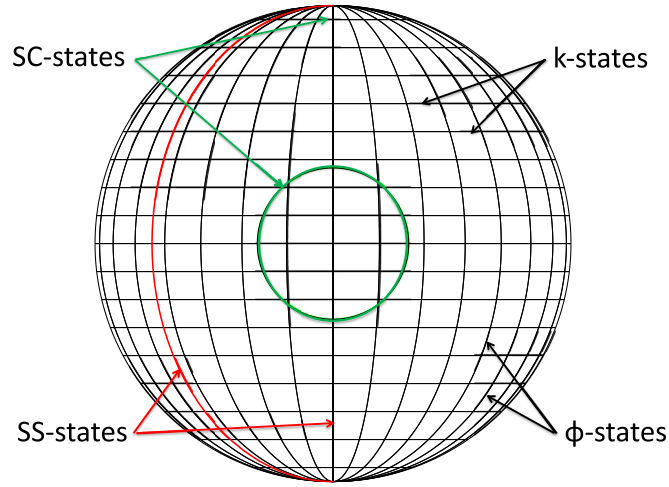

FIG. 1. Schematic illustration of the different states used as basis sets in the $\boldsymbol{j}$ space. Each state is represented by a curve along which the endpoint of angular momentum vector is distributed with equal probability. The k states are circles of constant latitude k. The ϕ states are semicircles of constant ϕ. The figure displays the pertaining meridians. For the continuous set of SCS only the states $|\theta = 0, \phi = 0\rangle$ and $|\theta = \pi/2, \phi = 0\rangle$ are shown. For the continuous set of SSS only the states $|\phi = 0\rangle$ and $|\phi = -\pi/4\rangle$ are shown.

The proposed SSS plots will be applied to the triaxial rotor and particle-rotor systems in this work in combination with the collective Hamiltonian introduced below.

B. Triaxial rotor model in angle-momentum representation

The classical mechanics of gyroscopes offers a framework for classifying quantal states. In this context, the classical orbits of the angular momentum vector, relative to the body-fixed principal axes, represent the intersection lines between the sphere of constant angular momentum and the ellipsoid of constant energy. Detailed discussions on the construction of these orbits can be found in Refs. [2,3,66]. For the triaxial rotor the orbits are given by the two angles θ and ϕ as

$$J_1 = \sqrt{I(I+1)}\sin\theta\cos\phi, \tag{11}$$

$$J_2 = \sqrt{I(I+1)}\sin\theta\sin\phi, \tag{12}$$

$$J_3 = \sqrt{I(I+1)}\cos\theta, \tag{13}$$

which are restricted to the sphere of constant angular momentum,

$$\boldsymbol{J}^2 = J_1^2 + J_2^2 + J_3^2 = I(I+1). \tag{14}$$

Namely θ is the angle between the angular momentum $\boldsymbol{J}$ and the 3-axis and ϕ is the angle between the projection of $\boldsymbol{J}$ onto the 1-2-plane and the 1-axis.

With the above definitions, the TRM Hamiltonian [1]

$$H_{\rm TR} = \frac{\hat{J}_1^2}{2\mathscr{J}_1} + \frac{\hat{J}_2^2}{2\mathscr{J}_2} + \frac{\hat{J}_3^2}{2\mathscr{J}_3} \tag{15}$$

can be rewritten as a classical Hamiltonian,

$$H_{\rm TR} = I(I+1)\left(\frac{\sin^2\theta\cos^2\phi}{2\mathscr{J}_1} + \frac{\sin^2\theta\sin^2\phi}{2\mathscr{J}_2} + \frac{\cos^2\theta}{2\mathscr{J}_3}\right), \tag{16}$$

which can be cast into the form

$$H_{\rm TR} = V(\phi) + \frac{J_3^2}{2B(\phi)}, \tag{17}$$

with

$$V(\phi) = I(I+1)\left(\frac{\cos^2\phi}{2\mathscr{J}_1} + \frac{\sin^2\phi}{2\mathscr{J}_2}\right), \tag{18}$$

$$B(\phi) = \frac{1}{2}\left[\frac{1}{2\mathscr{J}_3} - \frac{\cos^2\phi}{2\mathscr{J}_1} - \frac{\sin^2\phi}{2\mathscr{J}_2}\right]^{-1}. \tag{19}$$

In the above formula, the $\mathscr{J}_{1,2,3}$ are the corresponding moments of inertia of the three principal axes. It is crucial to highlight that the derivations presented above for the collective potential $V(\phi)$ and mass parameter $B(\phi)$ are carried out without any approximation. This rigorous treatment allows for a comprehensive and precise characterization of the quantum behavior associated with wobbling motion in triaxial nuclei.

The classical TRM Hamiltonian (17) in J_3-ϕ representation has the form of a kinetic term with the ϕ-dependent inertia parameter $B(\phi)$ and the periodic potential $V(\phi)$ as given by Eqs. (19) and (18). The step of quantization of the classical energy is not unique. To quantize it, we apply the general Pauli prescription [67,68]. The quantized form of the CH reads as [58–60]

$$H_{\rm CH} = -\frac{\hbar^2}{2\sqrt{B(\phi)}}\frac{\partial}{\partial\phi}\frac{1}{\sqrt{B(\phi)}}\frac{\partial}{\partial\phi} + V(\phi). \tag{20}$$

The volume element in the present collective space is

$$\int d\tau_{\rm CH} = \int_{-\pi}^{\pi} d\phi\sqrt{B(\phi)}. \tag{21}$$

The CH Hamiltonian is diagonalized in the basis

$$|\psi_K\rangle = \frac{1}{\sqrt{2\pi}}\frac{\exp[iK\phi]}{B^{1/4}(\phi)}. \tag{22}$$

The CH matrix elements are evaluated by numerical integration, where the derivation of $\partial/\partial\phi$ acts on the mass parameter term $B^{1/4}(\phi)$ in the denominator of Eq. (22). The results of the diagonalization in the basis $-I \leqslant K \leqslant I$ agrees exactly with the diagonalization of the original TRM Hamiltonian (15). It provides all solution with the four representations of the D_2 group $\mathscr{R}_1(\pi) = \pm 1$ and $\mathscr{R}_3(\pi) = \pm 1$. The TRM describes the rotational excitations built on the ground-state even-even nuclei. Therefore the intrinsic state is the quasiparticle vacuum, which has the symmetry $\mathscr{R}_1(\pi) = \mathscr{R}_3(\pi) = 1$. The TRM rotational states must have the same symmetry, because a rearrangement of the principal axes must leave the product of the intrinsic and rotational wave function invariant (see Ref. [1]). The Hamiltonian couples only basis states K with $K \pm 2$ and is invariant with respect to $K \to -K$. The completely symmetric representation corresponds to even-K and symmetric solutions for even-I and antisymmetric solutions for odd-I.

The collective function is written as

$$|\Psi\rangle_\nu = \sum_K C_{IK}^{(\nu)}|\psi_K\rangle, \tag{23}$$

in which the expansion coefficients $C_{IK}^{(\nu)}$ are obtained by diagonalizing the CH Hamiltonian (20) and used to construct the density matrix (8) to calculate the SSS plots. Additionally we diagonalized it in an extended K-basis, large enough that the results did not depend on the cutoff.

In order to derive the angle-momentum representation of the TR Hamiltonian, the authors of Refs. [44–46] used the SCS basis and accomplished the requantization by means of boson expansion techniques for the angular momentum operators. They studied approximate solutions of their version of the differential equation (20).

C. Collective Hamiltonian for the particle-triaxial-rotor model

The PTR model couples high-j particles to the triaxial rotor core. The corresponding Hamiltonian has been given in many textbooks, e.g., Ref. [1]

$$\hat{H}_{\rm PTR} = \hat{h}_p + \sum_{i=1,2,3} A_i\left(\hat{j}_i^2 - 2\hat{j}_i\hat{j}_i + \hat{j}_i^2\right). \tag{24}$$

with the inertial parameters $A_i = 1/(2\mathscr{J}_i)$. The particle Hamiltonian $\hat{h}_p$ is taken as single-j shell Hamiltonian

$$\hat{h}_p = \kappa\left[\left(3\hat{j}_3^2 - \boldsymbol{j}^2\right)\cos\gamma + \sqrt{3}\left(\hat{j}_1^2 - \hat{j}_2^2\right)\sin\gamma\right]. \tag{25}$$

The angle γ serves as the triaxial deformation parameter and the coupling parameter κ is proportional to the quadrupole deformation parameter β.

As discussed in our previous paper [3], the PTR Hamiltonian is diagonalized in the product basis $|IIK\rangle|jk\rangle$, where $|IIK\rangle$ are the rotational states for half-integer I and $|jk\rangle$ the high-j particle states in good spin j approximation. The eigenstates are hence expressed as

$$|II\nu\rangle = \sum_{K,k} C_{IKk}^{(\nu)}|IIK\rangle|jk\rangle. \tag{26}$$

The coefficients $C_{IKk}^{(\nu)}$ of the states in the triaxially deformed odd-A nuclei are not completely free. They are restricted by requirement that collective rotor states must be symmetric representations of the D_2 point group. When the K and k in the sum run respectively from $-I$ to I and from $-j$ to j, their difference $K-k$ must be even, and one half of all coefficients is fixed by the symmetry relation,

$$C_{I-K-k}^{(\nu)} = (-1)^{I-j}C_{IKk}^{(\nu)}. \tag{27}$$

From the amplitudes of the eigenstates $C^{(\nu)}_{IKk}$, the reduced density matrices

$$\rho^{(\nu)}_{kk'} = \sum_K C^{(\nu)}_{IKk} C^{(\nu)*}_{IKk'} \tag{28}$$

and

$$\rho^{(\nu)}_{KK'} = \sum_k C^{(\nu)}_{IKk} C^{(\nu)*}_{IK'k} \tag{29}$$

are obtained, which contain the information about the particle angular momentum $\boldsymbol{j}$ and the total angular momentum $\boldsymbol{J}$, respectively. The respective reduced density matrices are plugged into Eq. (7) to generate the pertaining SSS plots. We used the same method in our preceding paper [3] to generate the SCS plots.

In order to construct a CH we apply the adiabatic approximation. The particle angular momentum $\hat{j}_i$ is treated as an operator while the total angular momentum is treated as a classical vector as in Eqs. (11)–(13). The corresponding adiabatic Hamiltonian is written as

$$\hat{H}_{\rm ad} = \hat{h}_p + \sum_{i=1,2,3} A_i\big(J_i^2 - 2J_i\hat{j}_i + \hat{j}_i^2\big), \tag{30}$$

with J_i being numbers given in Eqs. (11)–(13) and the inertial parameters $A_i = 1/(2\mathscr{J}_i)$. The $\hat{H}_{\rm ad}$ is diagonalized in the $\boldsymbol{j}$-space $|jk\rangle$ (with k being the 3-axis component of the particle angular momentum $\boldsymbol{j}$ in the intrinsic frame). This indicates that the particle angular momentum operators $\hat{j}_i$ and $\hat{j}_i^2$ are treated exactly. The adiabatic approximation is similar but slightly different from the TAC mean-field approximation [58,61,69,70]. For the adiabatic PTR the recoil term $\langle\hat{j}_i^2\rangle$ is diagonalized, whereas it is replaced by $\langle\hat{j}_i\rangle^2$ under the TAC mean-field approximation.

The expectation value of the adiabatic Hamiltonian can be expressed in terms of the polar angle θ and azimuthal angle ϕ of the total angular momentum $\boldsymbol{J}$ as follows:

$$\begin{aligned}
E_{\rm ad}(\theta,\phi) &= \langle\hat{H}_{\rm ad}\rangle \\
&= \langle\hat{h}_p\rangle + \sum_{i=1,2,3} A_i\big(J_i^2 - 2J_i\langle\hat{j}_i\rangle + \langle\hat{j}_i^2\rangle\big) \\
&= \langle\hat{h}_p\rangle + \sum_{i=1,2,3} A_i\langle\hat{j}_i^2\rangle + I(I+1)[(A_1\cos^2\phi + A_2\sin^2\phi) + \cos^2\theta(A_3 - A_1\cos^2\phi - A_2\sin^2\phi)] \\
&\quad - 2\sqrt{I(I+1)}[A_1\sqrt{1-\cos^2\theta}\cos\phi\langle\hat{j}_1\rangle + A_2\sqrt{1-\cos^2\theta}\sin\phi\langle\hat{j}_2\rangle + A_3\cos\theta\langle\hat{j}_3\rangle].
\end{aligned} \tag{31}$$

We consider the TW case. The adiabatic energy has a minimum at $\theta = \pi/2$, because the long axis (3-axis) of the triaxial deformed nucleus has the smallest moment of inertia and the particles tend to align their angular momentum with the short axis (1-axis). In order to construct a CH of the form (17), we expand it with respect to $\cos\theta$, which is a small quantity near $\theta = \pi/2$. The linear term is zero because the expansion is around the minimum. Further employing the approximation

$$\sqrt{1-\cos^2\theta} \approx 1 - \tfrac{1}{2}\cos^2\theta, \tag{32}$$

one can approximate the adiabatic energy as

$$\begin{aligned}
E_{\rm ad}(\theta,\phi) &\approx \langle\hat{h}_p\rangle + \sum_{i=1,2,3} A_i\langle\hat{j}_i^2\rangle + I(I+1)(A_1\cos^2\phi + A_2\sin^2\phi) - 2\sqrt{I(I+1)}(A_1\cos\phi\langle\hat{j}_1\rangle + A_2\sin\phi\langle\hat{j}_2\rangle) - 2A_3J_3\langle\hat{j}_3\rangle \\
&\quad + J_3^2\left[(A_3 - A_1\cos^2\phi - A_2\sin^2\phi) + \frac{1}{\sqrt{I(I+1)}}(A_1\cos\phi\langle\hat{j}_1\rangle + A_2\sin\phi\langle\hat{j}_2\rangle)\right] \\
&= V(\phi) + \frac{J_3^2}{2B(\phi)},
\end{aligned} \tag{33}$$

where we have used Eqs. (11)–(13).

The collective potential $V(\phi)$ is energy $E_{\rm ad}(\theta = \pi/2, \phi)$. To obtain the mass parameter we calculate the energy variation generated by the very small shift $\delta = \theta - \pi/2$,

$$\Delta E = E_{\rm ad}(\pi/2 + \delta, \phi) - E_{\rm ad}(\pi/2, \phi). \tag{34}$$

Correspondingly, the angular momentum of the third component varies as

$$\Delta J_3^2 = J_3^2(\pi/2 + \delta, \phi) - J_3^2(\pi/2, \phi). \tag{35}$$

From the relationship

$$\Delta E = \frac{\Delta J_3^2}{2B(\phi)}, \tag{36}$$

one obtains

$$B(\phi) = \frac{\Delta J_3^2}{2\Delta E}. \tag{37}$$

One can easily check that using this method, the same mass parameter (19) of the TRM can be obtained.

D. Electromagnetic transition probabilities

The probability of the electromagnetic transitions $B(E2)$ can be obtained from the CH wave function expansion coefficients C^{ν}_{IK} on the basis ψ_K (22). The reduced $E2$ transition probability is calculated as

$$B(E2, I\nu \to I'\nu') = \sum_{\mu KK'} \left| C^{\nu'*}_{I'K'} C^{\nu}_{IK} \langle \psi_{K'} | \mathscr{M}^{E}_{2\mu} | \psi_K \rangle \right|^2. \quad (38)$$

The corresponding $E2$ operator is taken as

$$\mathscr{M}^{E}_{2\mu} = \sqrt{\frac{5}{16\pi}} \hat{Q}_{2\mu}, \quad (39)$$

$$\hat{Q}_{2\mu} = D^2_{\mu 0} Q'_{20} + \left(D^2_{\mu 2} + D^2_{\mu -2} \right) Q'_{22}, \quad (40)$$

with the intrinsic quadrupole moments

$$Q'_{20} = Q_0 \cos\gamma, \quad Q'_{22} = \frac{1}{\sqrt{2}} Q_0 \sin\gamma, \quad (41)$$

where Q_0 is the intrinsic charge quadrupole moment, calculated by $Q_0 = (3/\sqrt{5\pi}) R_0^2 Z\beta$, $R_0 = 1.2A^{1/3}$ fm. The matrix elements $\langle \psi_{K'} | \mathscr{M}^{E}_{2\mu} | \psi_K \rangle$ have the well-known form for good K states as given by Bohr and Mottelson [1].

III. RESULTS AND DISCUSSION

A. Triaxial rotor system

For the triaxial rotor, we discuss the system with the moments of inertia $\mathscr{J}_{m,s,l} = 30, 10, 5\ \hbar^2/\text{MeV}$ for the medium (m), short (s), and long (l) axes, which was studied previously in Refs. [2,3,35]. In Refs. [3,35], the energy spectra as function of spin and the angular momentum structure were illustrated in the framework of TRM. In addition, Ref. [3] introduced the two-dimensional SCS maps, i.e., probability distribution for the orientation of the angular momentum on the (θ, ϕ) plane, to extract the classical mechanics underpinning of the quantal triaxial rotor model from the numerical results. In this subsection, we will focus on discussing the information provided by the collective Hamiltonian and the one-dimensional SSS.

The calculated collective potential $V(\phi)$ and the collective mass parameter $B(\phi)$ for $I = 8$ are shown in Fig. 2. Note that ϕ is the angle between the projection of $\boldsymbol{J}$ onto the s-m plane and the s axis. The $V(\phi)$ and $B(\phi)$ are symmetrical with respect to $\phi = 0$ line, as a result of the invariance of the intrinsic quadrupole moments with respect to the D_2 symmetry for a triaxial rotor system. The minima in the $V(\phi)$ and $B(\phi)$ locate at $\phi = \pm\pi/2$, which corresponds to uniform rotation about the m axis with the largest moment of inertia.

Figure 2 further displays the TRM energies for states with angular momentum $I = 8$ and $I = 9$ as dots, while the energies obtained from the collective Hamiltonian are represented by bars. It is important to note that the D_2 symmetry imposes a restriction on the number of eigenstates. Specifically, for $I = 8$, there are five eigenstates labeled as $n = 0$, 2, 4, 6, and 8, while for $I = 9$, there are four eigenstates labeled as $n = 1$, 3, 5, and 7. Remarkably, the energies obtained from the collective Hamiltonian exhibit perfect agreement with those derived from the TRM calculations. This consistent agreement is expected because the derivation of the collective Hamiltonian, given by Eq. (20), does not introduce any approximations specifically for the triaxial rotor system. Consequently, the excellent agreement confirms the validity and accuracy of the collective Hamiltonian approach.

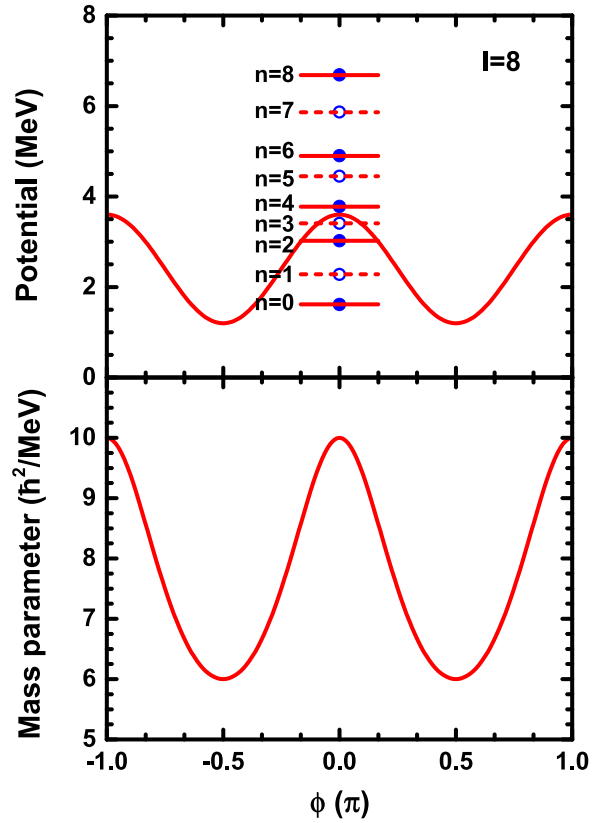

FIG. 2. Upper panel: Classical potential energy $V(\phi)$ as a function of ϕ for spin $I = 8$. The dots show the quantal energies E_v calculated by TRM, while the horizontal lines represent the energies obtained by the collective Hamiltonian H_{CH}, which incorporates a ϕ-dependent mass parameters $B(\phi)$ shown in the lower panel. Note that for the even-n states, they are calculated from $I = 8$ states, while for the odd-n states, they are calculated as the 72/90 of $I = 9$ energies.

The function $B(\phi)$ describing the collective potential does not depend on the spin, as shown in Eq. (19). However, the term $V(\phi)$ in the potential does depend on the spin through the factor $I(I+1)$, as described by Eq. (18). As a result, the stiffness of the collective potential increases with increasing spin. This characteristic has significant implications, as it suggests that the wobbling energy, defined as the energy difference between adjacent wobbling states, also increases with spin. This finding provides a more general perspective on the conclusion obtained by the assumption of small amplitude oscillations of the total angular momentum in the framework of TRM in Ref. [1].

As aforementioned, the SSS plots offer a quantum mechanical perspective by providing the probability density distribution of the wave function in the ϕ degree of freedom. These plots allow for an intuitive interpretation as they resemble the familiar probability density distributions in the

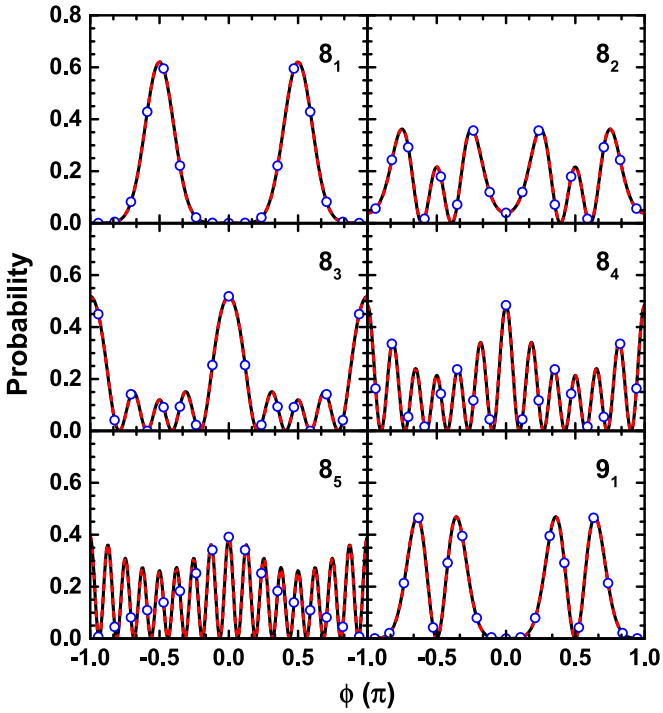

FIG. 3. Probability densities of the SSS for the triaxial rotor states 1–5 of $I = 8$ and the state 1 of $I = 9$. The smooth solid and dashed lines show the continuous SSS $P(\phi)_\nu$ obtained by the TRM and collective Hamiltonian, respectively. The dots represent the discrete SSS probability $\frac{2\pi}{2I+1}P(\phi_n)_\nu$.

ϕ representation. The probabilities of the SSS are illustrated in Fig. 3 for the triaxial rotor states numbered 1 to 5 with $I = 8$, as well as for state 1 with $I = 9$. These probabilities are calculated using the collective Hamiltonian and are compared with the corresponding probabilities obtained from the TRM calculations. Impressively, the resulting SSS plots obtained from the collective Hamiltonian calculations exhibit a high degree of agreement with those obtained from the TRM calculations. This agreement suggests that the SSS plots derived from the collective Hamiltonian can be interpreted as probability densities of the continuous eigenfunctions in the ϕ representation. Therefore, they provide a familiar and intuitive interpretation of the system's quantum mechanical properties.

In the classical regime, the motion of the triaxial rotor is confined to the regions between the potential energy function $V(\phi)$ and the bars, as depicted in Fig. 3. In the SSS plots, the $n = 0$ state denoted as 8_1 exhibits a prominent bump, which represents the presence of zero-point oscillations, arising from quantum mechanical fluctuations at the system's ground state. The $n = 1$ state labeled as 9_1 possesses the character of the first excited oscillator state. The ϕ oscillation has a larger amplitude, and a zero crossing at $\phi = \pm\pi/2$. This observation corresponds to the behavior of the Hermite polynomial H_1.

The $n = 2$ state, denoted as 8_2, exhibits the characteristics of the second oscillator state within the potential. The amplitude of the oscillation in the ϕ degree of freedom reaches almost π. Within the allowed regions of motion, there are two zeros symmetrically positioned at $\pm\pi/2$. This pattern reflects the Hermite polynomial H_2 in the wave function associated with this state.

The SSS plots corresponding to the states 8_3 ($n = 4$), 8_4 ($n = 6$), and 8_5 ($n = 8$) show a standing wave patterns with a periodicity of $2n$, where the potential energy function modulates the heights of the peaks. In particular, the $n = 8$ state 8_5 represents an almost pure $K_l = 8$ structure, with a relatively weak modulation which arises due to the interplay between the underlying potential energy landscape and the quantum mechanical properties associated with the state. For the $n = 4$ state 8_3, the SSS plot exhibits prominently enhanced peaks at $\phi = 0$ and π. This enhancement indicates the proximity of the classical separatrix orbit separating the wobbling motion with respect to the m axis and l axis. It represents the characteristic *flip* mode (FW) [3] that involves rapid transitions between the two orientations of the unstable s axis.

Figure 3 also includes the probability distribution of the discrete ϕ_n states, which is given by $\frac{2\pi}{2I+1}P(\phi_n)_\nu$ with a prefactor in order to properly normalize it. The SSS states smoothly interpolate between the discrete points of the ϕ_n distribution, resulting in a continuous wave function with a density distribution. However, the discreteness of the ϕ_n distribution tends to obscure the intuitive understanding of SSS structures, especially as the number of peaks increases. Particularly for the state 8_5, the discrete distribution appears counterintuitive. Since $K = 8$ is almost a good quantum number, one would expect the probabilities for all ϕ_n to be approximately equal. Contrary to this expectation, a decrease towards $\phi = \pm\pi$ is observed in the discrete ϕ_n distribution. This decrease is caused by the symmetrization of the state, specifically the superposition $(|IIK\rangle + |II - K\rangle)/\sqrt{2}$. This symmetrization leads to an interference between the $\phi_{\pm n}$ states. The continuous SSS density distribution, on the other hand, behaves as anticipated. It oscillates proportionally to $\cos^2(K\phi)$, while the envelope remains roughly constant. Therefore, the SSS plots highlights the interplay between continuous and discrete aspects of the quantum system and offers valuable insights into the symmetries and interference effects at play in the triaxial rotor system.

B. Particle-rotor system

For the particle-rotor system, we discuss ^{135}Pr reported in Refs. [14,15] as the first example for transverse wobbling of triaxial nuclei with normal deformation. In Ref. [2], the concepts of TW and LW were proposed in the framework of PTR using the tentative experimental result of ^{135}Pr as example. In Ref. [59], the suggested wobbling bands in ^{135}Pr were investigated using the collective Hamiltonian based on the TAC approach. The experimental energy spectra of both yrast and wobbling bands were well reproduced by the collective Hamiltonian. But the total angular momentum was not a good quantum number due to the rotational symmetry breaking in TAC. In Ref. [6], the behavior of the collective rotor in wobbling motion was investigated in PTR in the rotor angular momentum representation. In Ref. [3], the interpretation of the quantum states of the model of a triaxial rotor coupled to an odd-particle was discussed in detail using the wobbling motion in ^{135}Pr as example. In particular, two-dimensional

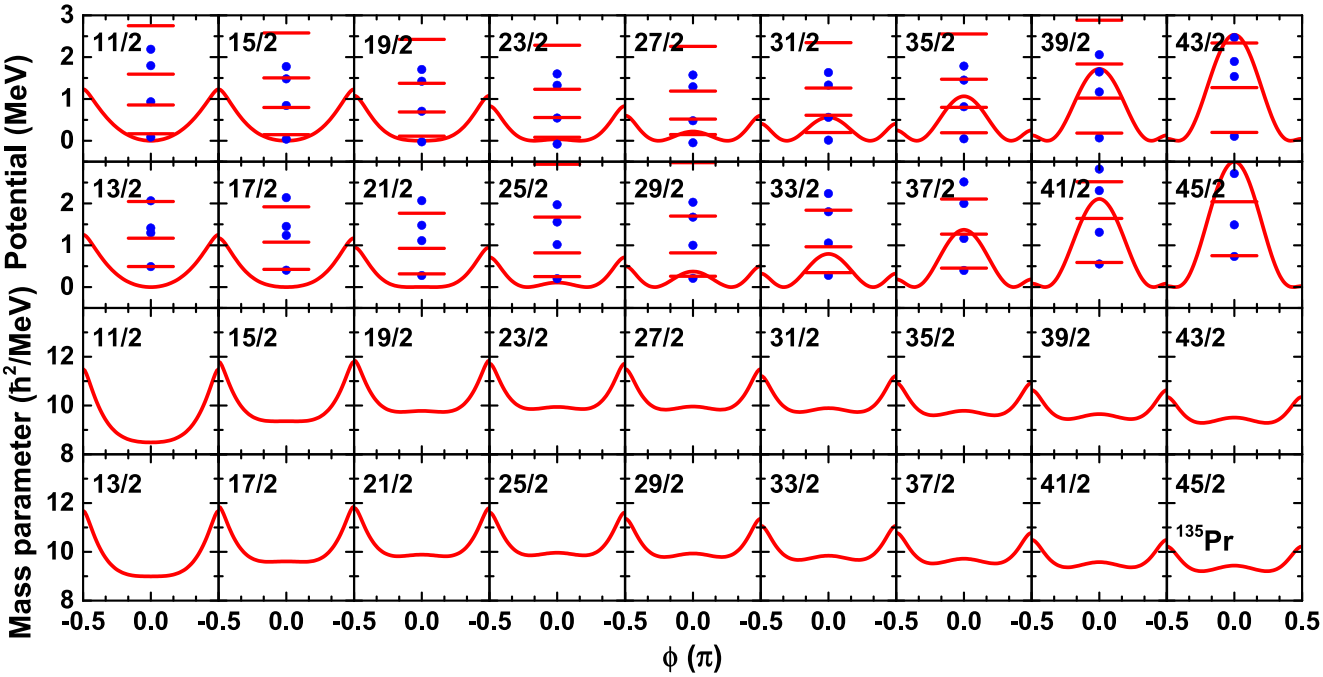

FIG. 4. Collective potential energy $V(\phi)$ (upper two panels) and mass parameter $B(\phi)$ (lower two panels) as functions of ϕ for the particle-rotor system of ^{135}Pr. The dots show the PTR energies $E_{\rm PTR}$, while the horizontal lines show the collective Hamiltonian energies $E_{\rm CH}$. Their energies are plotted with respect to the minima of the collective potential $E_{\rm ad}(\min)$.

plots of the probability distributions of the SCS were used to generalize the classification of the collective excitations of the PTR as TW and LW modes based on their topologies. In this subsection, we will show the results obtained by the collective Hamiltonian and the one-dimensional SSS.

The input parameters are $\beta = 0.17$ (corresponds to $\kappa = 0.038$), $\gamma = 26^\circ$, and $\mathscr{J}_{m,s,l} = 21,\ 13,\ 4\,\hbar^2/\text{MeV}$, the same as in Refs. [2,3,6].

To construct a collective Hamiltonian, similarly to the triaxial rotor case, we first calculate the collective potential and mass parameter starting from the adiabatic particle-rotor Hamiltonian (30). The adiabatic energy $E_{\rm ad}(\phi)$, which can be considered as the potential energy for the collective wobbling mode, is obtained by minimizing adiabatic energy $E_{\rm ad}(\theta,\phi)$ (33) with respect to the angles θ for fixed ϕ. The adiabatic energy $E_{\rm ad}(\phi) - E_{\rm ad}(\min)$ is displayed in Fig. 4, which represents the bottom of the valley in the surface $E_{\rm ad}(\theta,\phi)$ relative to its lowest point. To simplify the presentation, we focus on displaying the results within the region of $-\pi/2 \leqslant \phi \leqslant \pi/2$. However, it is important to note that the results in the regions of $-\pi \leqslant \phi \leqslant -\pi/2$ and $\pi/2 \leqslant \phi \leqslant \pi$ have symmetrical behavior with respect to the results in the region $-\pi/2 \leqslant \phi \leqslant 0$ and $0 \leqslant \phi \leqslant \pi/2$, respectively. This symmetry arises because the particle-rotor Hamiltonian is invariant under the D_2 symmetry.

As shown in Fig. 4, with increasing spin I the adiabatic energy becomes biased toward the m axis. Above the critical angular momentum $J_c = 11$ a maximum at $\phi = 0$ appears, which generates two minima with the same energy located at the angles $\pm\phi$.

The mass parameters $B(\phi)$ calculated by Eq. (37) are shown in Fig. 4 as well. As expected for a triaxial nucleus with D_2 symmetry, $B(\phi)$ is symmetric with respect to $\phi = 0$. The peaks of $B(\phi)$ at $\phi = \pm\pi/2$ drive the nucleus towards the m axis with the largest moment of inertia. Unlike in the case of the triaxial rotor system, the $B(\phi)$ in PTR changes with spin. The magnitude of $B(\phi)$ increases with spin in the low spin region $I \leqslant 29/2$, while decreases above $I = 31/2$.

The adiabatic potential allows one to associate a collective wave function with the wobbling mode, which provides a quantal perspective like the TRM wave function in Sec. III A. The CH

$$H_{\rm CH} = \frac{J_3^2}{2B(\phi)} + V(\phi) \tag{42}$$

is constructed by adding a kinetic term with the inertia parameter $B(\phi)$ to the potential energy $V(\phi)$ shown in Fig. 4. The CH is diagonalized in the discrete basis (22) with K being I, $I-2,\ldots,-I+1$. The pertaining amplitudes $C_{IK}^{(\nu)}$ represent the collective wave functions. For half-integer spin there are two degenerate states, because the CH couples only K with $K, K\pm 2$. They are

$$|\alpha_3\rangle = \sum_K C_{IK}^{(\nu)} |IIK\rangle, \quad |-\alpha_3\rangle = \sum_K C_{IK}^{(\nu)} |II-K\rangle,$$
$$K = I,\ I-2,\ \ldots,\ -I+1, \tag{43}$$

where $\alpha_3 = I$ is the signature with respect to $\mathscr{R}_3(\pi)$. The two solutions are related by time reversal and represent examples of Kramer's degeneracy of half-integer spin systems. It is sufficient to study the $|\alpha_3\rangle$ states.

The diagonalization of the CH provides more solutions than the PTR, because the latter takes into account that the TR rotor core states are the completely symmetric representations

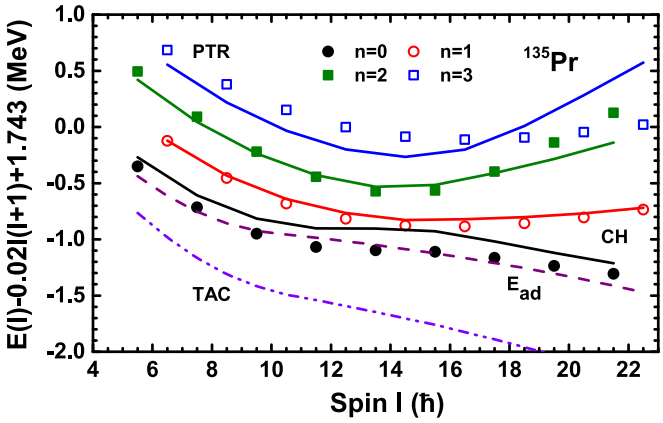

FIG. 5. Energies of the lowest states E_ν of the PTR Hamiltonian (symbols) and the collective Hamiltonian (full drawn lines), the adiabatic energy (dashed) and the TAC energy (dashed-dotted), for ^{135}Pr. The energies are shifted by 1.743 MeV, which is the lowest energy from the diagonalization of $h_p(\gamma)$ in Eq. (25). In the following, the yrast states ($n = 0$) are denoted by $11/2_1$, $15/2_1$, $19/2_1, \ldots$, the single wobbling excitations ($n = 1$) by $13/2_1$, $17/2_1$, $21/2_1, \ldots$, and the double wobbling excitations ($n = 2$) by $15/2_2$, $19/2_2$, $23/2_2, \ldots$.

of the D_2 group. This entangles the quantum state of the particle with the rotational state. The symmetry restriction gets lost in deriving the CH. In the quantal PTR version of Eq. (30) the Coriolis matrix elements $2\hat{J}_i\hat{j}_i$ couple the components $|IIK\rangle|jk\rangle$ in such a way that the change of the particle j projection k and the total J projection K are related such the core is total symmetric with respect to D_2. This correlation gets lost when $\hat{J}_i$ is replaced by the number J_i in calculating the adiabatic energy surface (30).

Comparing with the PTR solutions, one finds that for the signature $I = j + 2m$ (m being an integer number) the first and third solutions describe the $n = 0$ and $n = 2$ wobbling states. The second and fourth solutions should be discarded. These states with the $n = 1$ and $n = 3$ character do not appear in the PTR calculations. Likewise, for the signature $I = j + 1 + 2m$ the second and fourth solutions describe the $n = 1$ and $n = 3$ wobbling states. The first and second solutions should be discarded. These states with the $n = 0$ and $n = 2$ character do not appear in the PTR calculations.

The resulting energies of the lowest bands, which represent the $n = 0$, 1, 2, 3 wobbling states, agree rather well with the PTR values as displayed in Fig. 5. The $n = 0$ yrast states are 0.1–0.2 MeV too high. A possible reason is that from $E_{\rm ad}$(min), which is shown as the dashed line in Fig. 5, a "fluctuation term" should be subtracted, which generally appears in adiabatic collective Hamiltonians. In our case, it is attributed to the quantual fluctuations of the total angular momentum that are missed in the adiabatic potential, which is obtained for a fixed classical vector $\boldsymbol{J}$. Such corrections generally decrease the adiabatic potential, which would shift the dashed line in Fig. 5 somewhat below the PTR yrast energies (as well as the whole CH spectrum somewhat down). A comparison of the different contributions to the total energy shows that the PTR has a Coriolis term (negative) arising from fluctuations of the l component of $\boldsymbol{J}$, which are missing in the adiabatic energy.

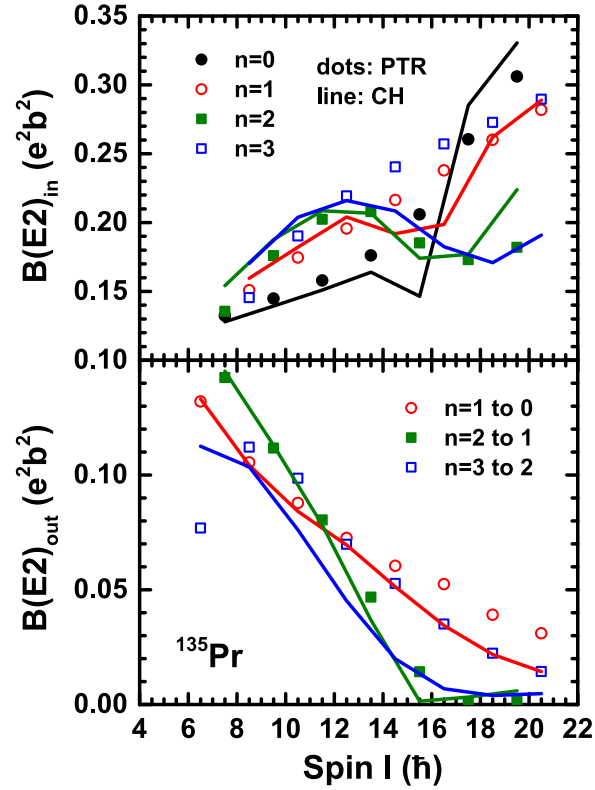

FIG. 6. Upper panel: Calculated in-band $B(E2)_{\rm in}(I \to I-2)$ of the bands in Fig. 5, where the same line and color conventions are used. Lower panel: Calculated interband $B(E2)_{\rm out}(I \to I-1)$ transition probabilities between the bands shown in Fig. 5. In order to keep the legend compact, the connecting transitions are labeled by quanta numbers n, which are associated with the oscillator states in the TW regime. Beyond, n represents just a counting label for the states.

The dots and horizontal lines in Fig. 4 show the energies with respect to the potential's minimum,

$$E_w = E_\nu - E_{\rm ad}(\min), \tag{44}$$

where E_ν are the energies calculated by the exact diagonalization of the PTR Hamiltonian or the CH. The minimum of the adiabtic energy $E_{\rm ad}$(min), is shown as the dashed line in Fig. 5. The energy difference (44) can be assigned to the collective wobbling energy.

One notes that the PTR states for spins $19/2$, $23/2$, and $27/2$ are located a bit below the minimum potential energy as shown in Fig. 4. This reflects the above discussed somewhat too-high energy of the adiabatic potential.

The upper panel of Fig. 6 compares the CH intraband $B(E2)_{\rm in}(I \to I-2)$ values with the PTR ones, where the same line convention as in Fig. 5 is used. The lower panel shows the interband $B(E2)_{\rm out}(I \to I-1)$ transition probabilities among the $n = 0$, 1, 2, and 3 bands in Fig. 5. The strong collective $\Delta I = 1$ $E2$ transitions, which characterize the wobbling motion, are reflected by Fig. 6. The CH results become inaccurate around $I = 33/2$, indicating that the adiabatic approximation is no longer good. For the $n = 3$ band the adiabatic approximation is also not good enough.

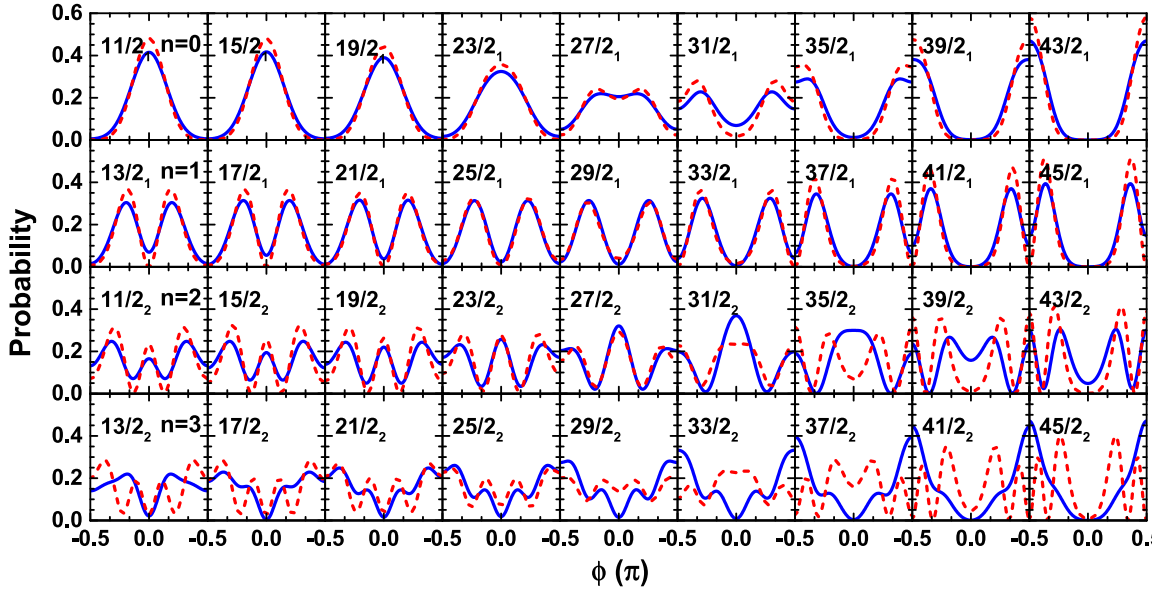

FIG. 7. Full curves show the probability density of the SSS for the $n = 0{-}3$ states calculated by PTR, while the dashed curves display the ones by the CH.

The SSS collective (SSS-CH) probability densities are calculated as the square of the collective wave function Eq. (23) obtained from the pure density matrices of the α_3 solutions. Using the $-\alpha_3$ solutions gives the same results.

Figure 7 compares these SSS-CH probability densities with the SSS PTR (SSS-PTR) densities directly obtained from the PTR reduced density matrices. Like for the TRM (see Sec. III A), we also diagonalized the collective Hamiltonian within a sufficiently extended basis of $|K| > I$ states. The results agree with ones shown in Figs. 4–7 on the scale of the figures. Hence one can see the SSS-CH densities as the probability densities of collective wave functions in the continuous ϕ approximation.

For the states $n = 0$ and $n = 1$, SSS-PTR probabilities are rather similar to the SSS-CH densities. This demonstrates that the development of the structure is well accounted by the collective Hamiltonian composed of the adiabatic double-well periodic potential and a kinetic term with a ϕ-dependent inertia parameter. The analog Hamiltonian describes the relative "pseudorotation" of the two parts of a molecule attached to each other by one chemical bond (see, e.g., Ref. [71]), where the collective wave functions are characteristic for double-well periodic potentials. The probability distributions in ϕ direction are standing waves with one, two, three, and four maxima in the interval $-\pi/2 \leqslant \phi \leqslant \pi/2$ for $n = 0,\ 1,\ 2,\ 3$, respectively. Within the full range $-\pi \leqslant \phi \leqslant \pi$ the maxima are located symmetrically to $\phi = 0,\ \pm\pi/2,\ \pm\pi$. Depending on the position of the potential minimum, the maxima form pairs close to $\phi = 0,\ \pm\pi$ in the case of TW and $\phi = \pm\pi/2$ in the case of LW.

The SSS-PTR densities correlate well with the SSS-CH ones of the $n = 0$ and 1 collective states. The $n = 2$ double wobbling structure is strongly disturbed yet recognizable. For $n = 3$ the SSS density substantially deviates from the CH one. The adiabatic approximation, on which the concept of a collective wave function is based, becomes progressively inaccurate with increasing n.

There is a complementary perspective. In calculating the reduced density matrix, the tracing out of the $\boldsymbol{j}$ degree of freedom destroys to some extend the coherence of the complete PTR wave function. In general, the properties of the $\boldsymbol{J}$ degrees of freedom are described by the reduced density matrix, which cannot be further simplified. If $\boldsymbol{j}$ follows $\boldsymbol{J}$ in an adiabatic way, the reduced density matrix can be approximated by a pure density matrix generated from a collective wave function in the $\boldsymbol{J}$ degree of freedom. The coherence in the $\boldsymbol{J}$ degree of freedom decreases with increasing n. One can quantify the degree of coherence by diagonalizing the reduced density matrix. For a pure, completely coherent state one eigenvalue is 1 and all other are zero. The TRM states are examples. For partial coherence one has one large eigenvalue, the eigenvector of which represents the coherent wave function and the eigenvalue its probability. The remaining eigenfunctions, which appear with the probability of their small eigenvalues, distort the coherence.

1. The TW regime

For $I \leqslant 23/2$, the collective potential has a minimum at $\phi = 0$. The SSS-PTR probability distributions in Fig. 7 are similar to the SSS-CH of the collective wave functions with $n = 0$, 1, and 2 within the adiabatic potential which is centered at $\phi = 0$. The densities have n pronounced maxima symmetric to $\phi = 0$, which reflect the Hermite polynomials H_n. The behavior is analogous to that of the TRM discussed in the context of Figs. 2 and 3. With increasing n, the SSS-PTR distributions appear progressively washed out as compared to the SSS-CH distributions of the collective wave functions. We attribute this to a loss of coherence which signals that the

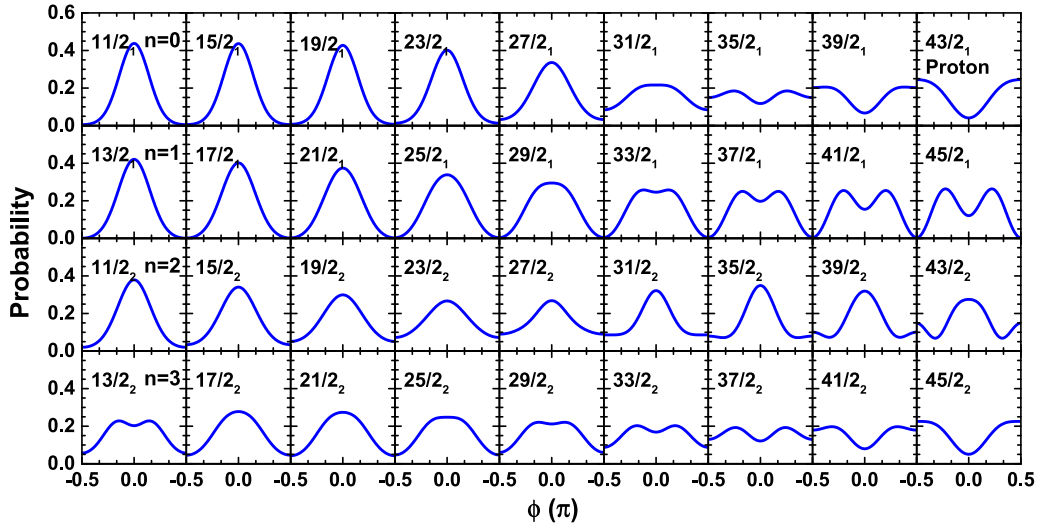

FIG. 8. The SSS probability density for the odd particle calculated by PTR for the $n = 0{-}3$ states.

adiabatic approximation loses accuracy. Figure 7 shows that the $n = 3$ PTR structures are not well described by the CH.

The SSS-PTR distribution of state $n = 3$ substantially deviates from the SSS-CH of the collective wave functions, which indicates that the adiabatic approximation fails. This can be seen comparing the SSS distribution for the odd particle in Fig. 8. As expected for the adiabatic behavior, the particle is well aligned with the s axis for $n = 0$, 1, and 2. The $n = 3$ distribution is different. We associated the difference with the mixing of the $n = 3$ collective wobbling state and the signature partner band. The latter represents the first excited state of the adiabatic Hamiltonian (30), which is not taken into account when deriving the CH.

For the $n = 3$ states $17/2_2$, $21/2_2$, and $25/2_2$, the adiabatic condition is as badly realized as for $13/2_2$. The SSS distributions for $\boldsymbol{j}$ are nearly the same as for $13/2_2$ and $25/2_2$ in Fig. 8. The SSS-PTR densities for $\boldsymbol{J}$ resemble the SSS-CH qualitatively. The classification of the states as strongly perturbed three-quanta TW oscillations seems acceptable. In our preceding paper we argued that the coupling of the $n = 3$ wobbling state with the signature partner state becomes weaker with increasing I.

Up to $I = 23/2$, the $n = 0$ SSS distributions have a peak at $\phi = 0$, which gets wider with I. As expected for TW, the wobbling energy

$$E_w(I) = E(I,\ n = 1) - \tfrac{1}{2}[E(I-1,\ n = 0) + (I+1,\ n = 0)] \tag{45}$$

decreases with I. The PTR transition probabilities in Fig. 6 are well reproduced by the CH states.

2. The flip regime

For $I = 27/2$-$35/2$, the potential develops a maximum at $\phi = 0$, which generates two minima near $\phi = \pi/4$. The $n = 0$ states $27/2_1$ and $31/2_1$ can be interpreted as being composed of two states localized in the two minima (localized states), which are coupled by tunneling through the shallow barriers. The superposition of the localized states is constructive as seen by the substantial SSS probability under the barriers. With increasing I, the tunneling through the barriers at $\phi = 0$ decreases and the tunneling through the barriers at $\pm\pi/2$ increases, which reflects the respective change of the barrier heights. For $I \geqslant 35/2$, the SSS plots are well understood in terms of the even $n = 0$ and odd $n = 1$ wave functions in a collective potential with an increasing barrier at $\phi = 0$ and a decreasing small hump at the m axis. The $n = 1$ states $29/2_1$ and $33/2_1$ represent the odd linear composition of the local states. They are little sensitive to the presence of the barriers at $\phi = \pm\pi/2$, because their probability is small there, where the wave functions changes sign.

The SSS plots of the $n = 2$ states can be understood in terms of the probability densities of the collective wave functions belonging to the periodic potentials shown in Fig. 4. The SSS plots of the states $31/2_2$ and $35/2_2$ show two minima half-way between the s and m axes and two maxima located at the barriers (at $\phi = 0, \pm\pi/2$). The SSS plot of the state $43/2_2$ shows the characteristic two minima located symmetrically to $\phi = \pm\pi/2$, respectively. The SSS probability of state $29/2_2$ illustrates the transition from the TW to the flip mode (FM) and the one of the state of $39/2_2$ the transition from the FM to the LW mode.

There is another perspective. The vicinity of the barrier top slows down the motion, which is reflected by the large probability density. Accordingly, the vector $\boldsymbol{J}$ flips between the barrier tops like 8_3 state of the TRM, which is close to the separatrix.

3. The LW regime

For the states $37/2_1$, $39/2_1$, $41/2_1$, and $45/2_1$, the adiabatic potential in Fig. 4 has deep minima centered around $\phi = \pm\pi/2$ with a tiny bump in the middle. The SSS-CH distributions follow well the SSS-PTR ones. The states have the nature of $n = 0$ and 1 LW wobbling vibrations around $\phi = \pm\pi/2$. The LW character is not generated by the "frozen alignment" of the proton angular momentum $\boldsymbol{j}$ with the m axis. Figure 9 shows the adiabatic angle φ of the particle

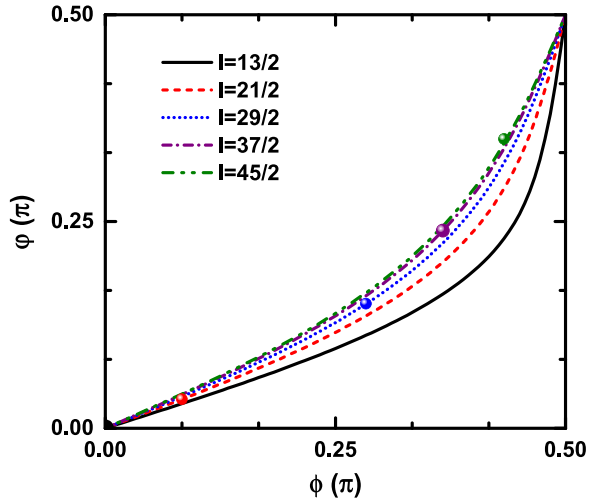

FIG. 9. The azimuthal angle φ of $\boldsymbol{j}$ as a function of azimuthal angle ϕ of $\boldsymbol{J}$ obtained by diagonalization of $H_{\rm ad}$ for the selected spins $I = 13/2, 21/2, 29/2, 37/2$, and $45/2$. The dot on the curve label the potential minimum for each spin.

vector $\boldsymbol{j}$ as function of the angle ϕ of the total angular momentum $\boldsymbol{J}$. In case of the high I values of the LW regime, $\boldsymbol{j}$ is pulled toward $\boldsymbol{J}$ by the Coriolis force, but $\varphi < \phi$ due to the triaxial potential, which favors $\varphi = 0$. This explains the SSS plots in Fig. 8. They show the same kind of maxima as the SSS-PTR. However, the corresponding maxima are wider and shifted toward $\varphi = 0$. The difference is understood by means of Fig. 9.

For the states $33/2_2$, $37/2_2$, $41/2_2$, and $45/2_2$, the PTR and CH SSS densities differ qualitatively from each other. As expected, the SSS-CH develops into a $n = 3$ LW structure with three minima located symmetrically to $\phi = \pm\pi/2$. In contrast, the maxima of the SSS-PTR distribution at $\phi = \pm\pi/2$ become dominant and the oscillations disappear. This indicates a change of the structure, which is beyond the realm of adiabaticity. As seen in Fig. 8, the particle SSS has a maximum whereas the SSS-PTR has a minimum, i.e., $\boldsymbol{j}$ and $\boldsymbol{J}$ move with opposite phase, which is not uncommon for higher excited states of coupled oscillators.

C. Two-quasiarticle-rotor system

In the study of two-quasiparticle-rotor system, the even-even nucleus ^{130}Ba has been identified as the first example of a system exhibiting two-quasiparticle wobbling bands [22,23]. The authors of Ref. [22] observed two new bands built on the two-quasiparticle $\pi(1h_{11/2})^2$ configuration in ^{130}Ba. In Ref. [23], these two bands were investigated using the constrained triaxial covariant density functional theory (CDFT) combined with quantum PTR calculations. The energy difference between the two bands, as well as the available electromagnetic transition probabilities $B(M1)_{\rm out}/B(E2)_{\rm in}$ and $B(E2)_{\rm out}/B(E2)_{\rm in}$, were well reproduced. The analysis of the angular momentum geometry demonstrated that lower band, the well-known S-band, represents the zero-quanta TW oscillation and the higher band represents the one-quanta TW oscillation state generated by a two-quasiparticle configuration. Later, the two-quasiparticle wobbling in ^{130}Ba was further examined using the projected shell model [24], providing additional support for this phenomenon. In the following, we use this example to discuss its interpretation in terms of the SSS visualization and a collective Hamiltonian.

In the investigation of the two-quasiparticle $\pi(1h_{11/2})^2$ configuration in ^{130}Ba [23], the deformation parameters were determined to be at a triaxial shape characterized by ($\beta = 0.24$, $\gamma = 21.5^\circ$) using constrained triaxial CDFT calculations. In order to model this triaxial rotor system, three spin-dependent moments of inertia $\mathcal{J}_i = \Theta_i(1 + cI)$ were introduced, where $i = s$, m, and l. The parameters $\Theta_{s,m,l} = 1.09$, 1.50, and 0.65 $\hbar^2$/MeV and $c = 0.59$ were determined by adjusting the PTR energies to the experimental energies of the $n = 0$ and 1 bands [23].

The approach is analogous to the treatment of the one-particle case [Eq. (30)], except the adiabatic Hamiltonian (30) is diagonalized in the space of the two-quasiparticle configurations. The adiabatic potential $V(\phi) = E_{\rm ad}(\phi) - E_{\rm ad}(\min)$ and the mass parameter $B(\phi)$ are depicted in Fig. 10. As the spin I increases, the adiabatic energy becomes increasingly favored along the m axis, similarly to the case of ^{135}Pr shown in Fig. 4. Beyond the critical angular momentum of $J_c = 22$, a maximum at $\phi = 0$ emerges, resulting in the presence of two minima with equal energy at angles $\pm\phi$. Compared to ^{135}Pr, the transverse geometry in ^{130}Ba exhibits greater stability and is sustained over a much wider range of spin values. The increased stability can be attributed to the larger angular momentum aligned with the s axis, which is generated by two quasiprotons instead of one.

The mass parameter $B(\phi)$ is also presented in Fig. 10. Its magnitude increases with increasing spin and is generally larger than the one of ^{135}Pr. This enhancement in the magnitude of $B(\phi)$ can be attributed to the larger alignment along the s axis caused by the presence of two protons. The two protons contribute significantly to the overall dynamics of the system, thus influencing the wobbling behavior.

The CH is diagonalized in the discrete basis (22) with even K being $I, I-2, \ldots, -I$ for the even-I and $I-1, I-3, \ldots, -(I-1)$ for the odd-I. The resulting energies come in close pairs. For even-I the first, third, and so on, solutions are associated with the $n = 0$, 2,... PTR wobbling states. For odd-I the third, fifth, and so on, solutions are associated with the $n = 1$, 3,... PTR wobbling states. The selection can be justified by direct comparison with the PTR solutions.

As the CH couples only K with $K \pm 2$, there is a complementary set of solutions obtained by diagonalizing the CH in the basis of odd-K. The energies turn out to be very close to the energies of the even-K solutions. The pertaining SSS plots are indistinguishable from the ones of the even-K ones on the scale of Fig. 13. The full PTR state is composed of both even- and odd-K components. Thus the difference between the two types is a consequence of approximation scheme. For this reason, the odd-K solutions will be disregarded as well.

Figure 11 compares the PTR energies with the adopted CH energies. The agreement is better than in the case of ^{135}Pr. Only the $n = 2$ states are somewhat too low. The CH potentials in Fig. 10 indicate that in ^{130}Ba the TW regime

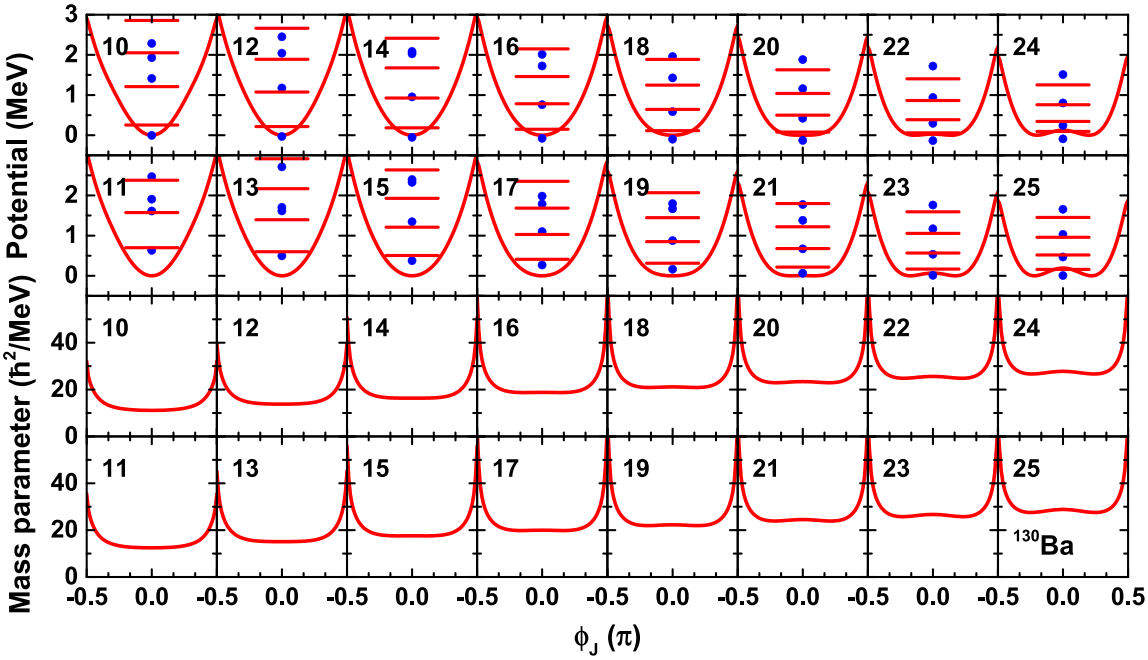

FIG. 10. Same as Fig. 4, but for the case of ^{130}Ba.

extends to $I = 22$ where the flip regime begins. Accordingly, the energies change from the equidistant harmonic TW spectrum at low I to $E_w \approx 0$ at $I = 24$, which indicates the instability of TW. The adiabatic approximation very well accounts for the structural change.

In Fig. 12, the upper panel displays the in-band $B(E2)_{\rm in}(I \to I-2)$ transition probabilities for the bands presented in Fig. 11, where the same line conventions are employed. The lower panel exhibits the interband $B(E2)_{\rm out}(I \to I-1)$ transition probabilities for the $n = 0$, 1, and 2 bands depicted in Fig. 11. It is noted that the wobbling motion's strong collective $\Delta I = 1$ $E2$ transitions are clearly evident in Fig. 12. The collective Hamiltonian describes very well the $B(E2)_{\rm in}(I \to I-2)$ PTR values. The $B(E2)_{\rm out}(I \to I-1)$ of the collective Hamiltonian are overall slightly smaller than those of PTR.

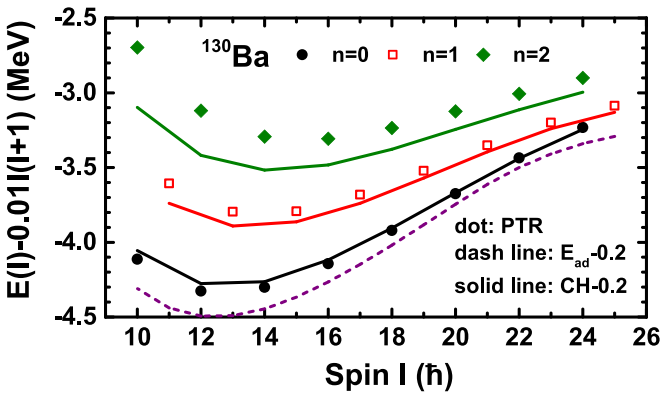

FIG. 11. Same as Fig. 5, but for the case of ^{130}Ba. Note that the energies obtained from the collective Hamiltonian are 0.2 MeV shifted down.

Figure 13 compares the SSS-CH probability densities calculated from the accepted collective wave functions with the SSS-PTR densities derived from the PTR reduced density matrices. Clearly, the adiabatic approximation works well for all

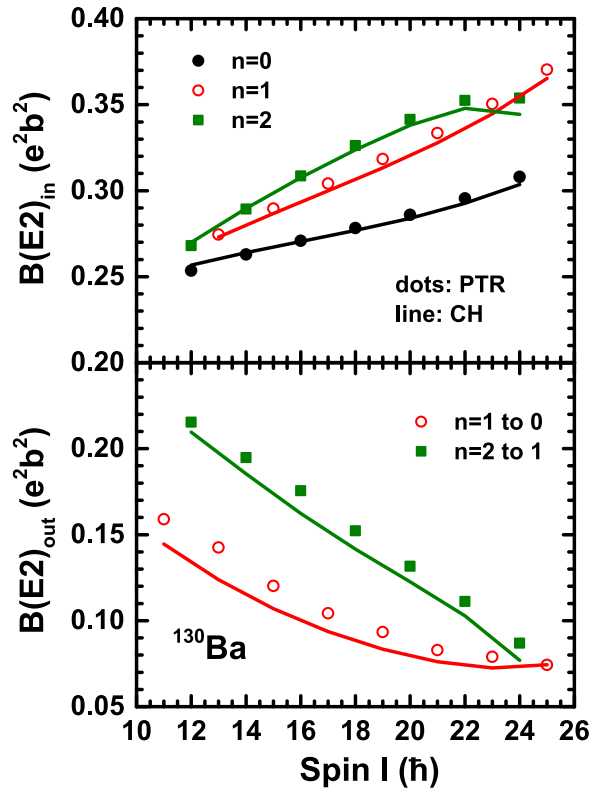

FIG. 12. Same as Fig. 6, but for the case of ^{130}Ba.

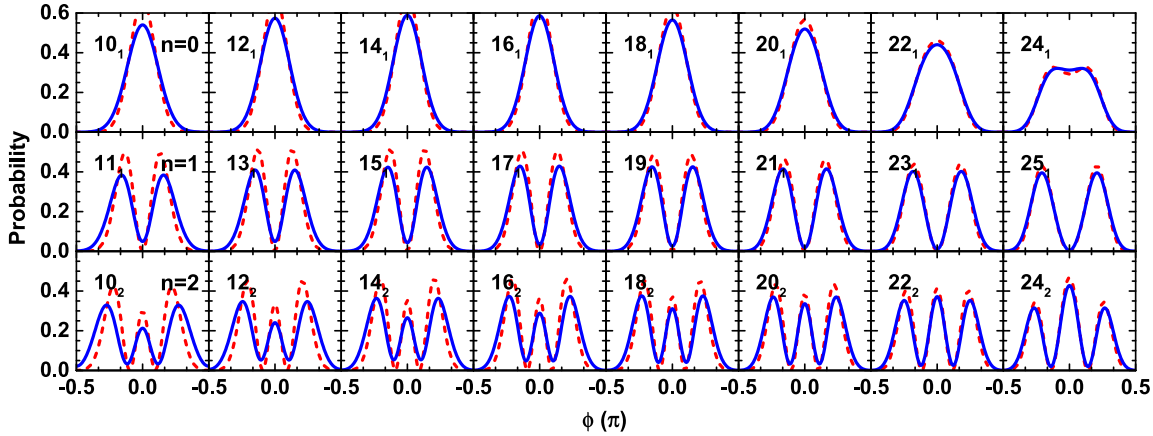

FIG. 13. Same as Fig. 7, but for the case of ^{130}Ba.

cases. The distinctive features associated with the wobbling states $n = 0$, 1, and 2 manifest themselves as the increasing number of minima symmetrically situated around $\phi = 0$. They reflect the Hermit polynomials which characterize the number of excitation quanta in the system.

The remarkable correspondence between the SSS-PTR densities and the SSS-CH densities affirms that the structural evolution can be effectively described by the collective Hamiltonian, which comprises the adiabatic double-well periodic potential and a kinetic term incorporating a ϕ-dependent inertia parameter. Hence, it can be concluded that the implementation of SSS-plots in the analysis of the one-quasiparticle-rotor and two-quasiparticle-rotor systems leads to intuitive and comprehensive understanding of the underlying phenomena.

D. Collective Hamiltonian based on tilted axis cranking

Figure 5 also includes the energy of the $n = 0$ band calculated by means of the TAC approach. The total Routhian

$$\hat{H}_{\rm TAC} = \hat{h}_p - \omega(\cos\phi\,\hat{j}_1 + \sin\phi\,\hat{j}_2) - \tfrac{1}{2}\mathscr{J}_1\omega^2\cos^2\phi - \tfrac{1}{2}\mathscr{J}_2\omega^2\sin^2\phi \qquad (46)$$

is diagonalized for a grid of cranking frequency ω and tilt angle ϕ values, which gives the Routhian $E'_{\rm TAC}(\omega,\phi)$ as the lowest eigenvalue and the pertaining classical angular vector components

$$J_1(\omega,\phi) = \langle\hat{j}_1\rangle + \omega\cos\phi\,\mathscr{J}_1, \qquad (47)$$

$$J_2(\omega,\phi) = \langle\hat{j}_2\rangle + \omega\sin\phi\,\mathscr{J}_2. \qquad (48)$$

For the above-discussed adiabatic energy the recoil term $\langle\hat{j}_i^2\rangle$ is diagonalized. It is replaced by $\langle\hat{j}_i\rangle^2$ under the TAC mean-field approximation. In TAC the total angular momentum J is constrained to be $\sqrt{I(I+1)}$ by adjusting the cranking frequency ω. The difference between the TAC energy and $E_{\rm ad}$ are almost constant 0.3 MeV in the whole spin region. That is, up to this shift the classical energy is the same as the PTR adiabatic energy, and the CH based on the TAC classical energy is nearly the same as well.

The authors of Refs. [58,59] calculated the TAC energy and used the Routhian as the collective potential $V(\phi) = E'_{\rm TAC}(\omega,\phi)$ for a fixed value of the frequency ω. The mass parameter was estimated using the frozen alignment (FA) approximation [2], namely a harmonic vibration around $\phi = 0$. Based on these, the CH method gives wobbling energies that are in agreement with the PTR values.

The success of the CH based on the TAC classical energy suggests applying the method developed for the PTR system to the microscopic versions of the TAC approach. The problem that the CH provides to many solutions will arise as well. The "exact" PTR solution which we used to select the appropriate solution will not be available in this case. In a future study of the CH based on the microscopic TAC we will discuss how the selection can be based on the analysis of the symmetry-broken states of the adiabatic Hamiltonian (30).

IV. SUMMARY

In summary, we introduced the SSS as a nonorthogonal and overcomplete basis. The utilization of SSS plots in the analysis of the particle-rotor system offers a new perspective into the angular momentum geometry and complex dynamics of the constituents by visualizing the system in terms of the familiar paradigm of a potential and a mass parameter for the orientation of the total angular momentum.

The semiclassical approach was combined with the adiabatic approximation in order to calculate the collective potential and mass parameters of a collective Hamiltonian (CH) capable of describing the wobbling motion in both even-even and odd-mass systems. The adiabatic approximation assumes that the response of the one or two particles can be calculated by classically rotating the triaxial potential they are moving within, which, in essence, amounts to the tilted axis cranking (TAC) method. The resulting energy as function of the orientation classical angular momentum vector $\boldsymbol{J}$ represents the classical CH when expressing it by the angle ϕ of $\boldsymbol{J}$ with the short axis and component J_l along the long axis, which represent a classical canonical pair of momentum and position respectively. Expanding about $J_l = 0$ up to second order results in the familiar form $J_l^2/B(\phi) + V(\phi)$.

The corresponding quantal CH is obtained by requantization according to the Pauli prescription.

By diagonalizing the CH, we obtained the energies, $E2$ transition probabilities, and state vectors, which were compared with the exact ones from the diagonalization of the original one- and two-particle plus triaxial rotor (PTR) Hamiltonian. In order to compare the structure of the PTR states with the structure of the CH states we employed the probability density $P(\phi)$ of the respective the SSS states, which corresponds to the conventional probability density of a wave function.

Good agreement between the of the results from the CH and PTR was found for the yrast states and the first and second states above yrast. This is a proof of principle that the construction of the CH from the adiabatic energy can be applied to the microscopic TAC calculations. One can expect that the $n = 0$, $n = 1$ and, with some reservation, the $n = 2$ wobbling excitations will be described by such an extension of the TAC method. Work along these lines is planned.

Interpreting the plots of the SSS probability density as the probability density of collective wave functions associated with the collective classical periodic potential $V(\phi)$ (equal to the adiabatic classical energy) provides a classification scheme for the PTR states based on their similarity with their with the CH states, which was introduced in our previous study [3]. There the geometry of the SCS proxies of the classical orbits were used, here we invoked the familiar "potential + kinetic energy" paradigm of wave functions.

By fixing the energy to one of the PTR states, the classical motion is confined to stay within $V(\phi)$, which provides a straightforward topological classification. For the TW mode the allowed region is centered around one of the axes perpendicular to the medium axis with the largest moment of inertia. For the LW mode the allowed region is centered around the medium axis itself. For the considered cases of one or two particles at the bottom of a high-j shell, with increasing angular momentum $V(\phi)$ changes from being centered around the short axis ($\phi = 0, \pm\pi$) to being centered around the medium axis ($\phi = \pm\pi/2$). That is, the mode changes from TW to LW. In the transition region the potential minima are located around $\phi = \pm\pi/4$, $\pm 3\pi/4$. The lowest states represent FM where the angular momentum vector jumps between different regions of the potential landscape. For the $n = 0$ state it flips between the minima with no phase change. For the $n = 1$ state it flips between the minima with a phase change. For the $n = 2$ state, when the energy of the system is close to the tops of the potential, barriers, the angular momentum vector flips between these locations.

For our example of ^{135}Pr, the SSS plots calculated by the exact PTR model correlate very well with the probability densities of the wave functions that belong to the CH. One recognizes the TW, LW, and transitional FW pattern implied by the collective Hamiltonian for $n = 0$, 1 wobbling states. For the $n = 2$ state the exact density profile shows the triple maxima of the collective wave function in the TW and LW regime. However, it deviates from the flip profile of the CH between the potential barriers. The exact profile of the next excitation differs qualitatively from the $n = 3$ structure of the CH. The increasing deviations with n of the SSS plots of the collective wave functions from the exact ones reflect the expected deterioration of the adiabatic approximation with the excitation energy.

For the second example of ^{130}Ba with two protons in the system, the TW geometry exhibits greater stability and is sustained over a much wider range of spin values. The flip regime is encountered at the maximal observed angular momentum of $I = 24$. For the less stable case of ^{135}Pr the experimental data cover the transition from TW to LW.

ACKNOWLEDGMENT

This work was supported by the National Natural Science Foundation of China under Grant No. 12205103 and the U.S. DoE Grant No. DE-FG02-95ER40934.

[1] A. Bohr and B. R. Mottelson, *Nuclear Structure* (Benjamin, New York, 1975), Vol. II.
[2] S. Frauendorf and F. Dönau, Phys. Rev. C **89**, 014322 (2014).
[3] Q. B. Chen and S. Frauendorf, Eur. Phys. J. A **58**, 75 (2022).
[4] F. Q. Chen, Q. B. Chen, Y. A. Luo, J. Meng, and S. Q. Zhang, Phys. Rev. C **96**, 051303(R) (2017).
[5] Q. B. Chen and J. Meng, Phys. Rev. C **98**, 031303(R) (2018).
[6] E. Streck, Q. B. Chen, N. Kaiser, and Ulf.-G. Meißner, Phys. Rev. C **98**, 044314 (2018).
[7] P. Bringel, G. B. Hagemann, H. Hübel, A. Al-khatib, P. Bednarczyk, A. Bürger, D. Curien, G. Gangopadhyay, B. Herskind, D. R. Jensen, D. T. Joss, T. Kröll, G. Lo Bianco, S. Lunardi, W. C. Ma, N. Nenoff, A. Neußer-Neffgen, C. M. Petrache, G. Schönwasser, J. Simpson, A. K. Singh, N. Singh, and G. Sletten, Eur. Phys. J. A **24**, 167 (2005).
[8] S. W. Ødegård, G. B. Hagemann, D. R. Jensen, M. Bergström, B. Herskind, G. Sletten, S. Törmänen, J. N. Wilson, P. O. Tjøm, I. Hamamoto, K. Spohr, H. Hübel, A. Görgen, G. Schönwasser, A. Bracco, S. Leoni, A. Maj, C. M. Petrache, P. Bednarczyk, and D. Curien, Phys. Rev. Lett. **86**, 5866 (2001).
[9] D. R. Jensen, G. B. Hagemann, I. Hamamoto, S. W. Ødegård, B. Herskind, G. Sletten, J. N. Wilson, K. Spohr, H. Hübel, P. Bringel, A. Neußer, G. Schönwaßer, A. K. Singh, W. C. Ma, H. Amro, A. Bracco, S. Leoni, G. Benzoni, A. Maj, C. M. Petrache, G. Lo Bianco, P. Bednarczyk, and D. Curien, Phys. Rev. Lett. **89**, 142503 (2002).
[10] G. Schönwaßer, H. Hübel, G. B. Hagemann, P. Bednarczyk, G. Benzoni, A. Bracco, P. Bringel, R. Chapman, D. Curien, J. Domscheit, B. Herskind, D. R. Jensen, S. Leoni, G. Lo Bianco, W. C. Ma, A. Maj, A. Neusser, S. W. Ødegård, C. M. Petrache, D. Rossach, H. Ryde, K. H. Spohr, and A. K. Singh, Phys. Lett. B **552**, 9 (2003).
[11] H. Amro, W. C. Ma, G. B. Hagemann, R. M. Diamond, J. Domscheit, P. Fallon, A. Gorgen, B. Herskind, H. Hübel, D. R. Jensen, Y. Li, A. O. Macchiavelli, D. Roux, G. Sletten, J. Thompson, D. Ward, I. Wiedenhover, J. N. Wilson, and J. A. Winger, Phys. Lett. B **553**, 197 (2003).

[12] D. J. Hartley, R. V. F. Janssens, L. L. Riedinger, M. A. Riley, A. Aguilar, M. P. Carpenter, C. J. Chiara, P. Chowdhury, I. G. Darby, U. Garg, Q. A. Ijaz, F. G. Kondev, S. Lakshmi, T. Lauritsen, A. Ludington, W. C. Ma, E. A. McCutchan, S. Mukhopadhyay, R. Pifer, E. P. Seyfried, I. Stefanescu, S. K. Tandel, U. Tandel, J. R. Vanhoy, X. Wang, S. Zhu, I. Hamamoto, and S. Frauendorf, Phys. Rev. C **80**, 041304(R) (2009).

[13] A. Mukherjee, S. Bhattacharya, T. Trivedi, S. Tiwari, R. P. Singh, S. Muralithar, Yashraj, K. Katre, R. Kumar, R. Palit, S. Chakraborty, S. Jehangir, Nazira Nazir, S. P. Rouoof, G. H. Bhat, J. A. Sheikh, N. Rather, R. Raut, S. S. Ghugre, S. Ali, S. Rajbanshi, S. Nag, S. S. Tiwary, A. Sharma, S. Kumar, S. Yadav, and A. K. Jain, Phys. Rev. C **107**, 054310 (2023).

[14] J. T. Matta, U. Garg, W. Li, S. Frauendorf, A. D. Ayangeakaa, D. Patel, K. W. Schlax, R. Palit, S. Saha, J. Sethi, T. Trivedi, S. S. Ghugre, R. Raut, A. K. Sinha, R. V. F. Janssens, S. Zhu, M. P. Carpenter, T. Lauritsen, D. Seweryniak, C. J. Chiara, F. G. Kondev, D. J. Hartley, C. M. Petrache, S. Mukhopadhyay, D. V. Lakshmi, M. K. Raju, P. V. Madhusudhana Rao, S. K. Tandel, S. Ray, and F. Dönau, Phys. Rev. Lett. **114**, 082501 (2015).

[15] N. Sensharma, U. Garg, S. Zhu, A. D. Ayangeakaa, S. Frauendorf, W. Li, G. Bhat, J. A. Sheikh, M. P. Carpenter, Q. B. Chen, J. L. Cozzi, S. S. Ghugre, Y. K. Gupta, D. J. Hartley, K. B. Howard, R. V. F. Janssens, F. G. Kondev, T. C. McMaken, R. Palit, J. Sethi, D. Seweryniak, and R. P. Singh, Phys. Lett. B **792**, 170 (2019).

[16] S. Biswas, R. Palit, S. Frauendorf, U. Garg, W. Li, G. H. Bhat, J. A. Sheikh, J. Sethi, S. Saha, P. Singh, D. Choudhury, J. T. Matta, A. D. Ayangeakaa, W. A. Dar, V. Singh, and S. Sihotra, Eur. Phys. J. A **55**, 159 (2019).

[17] N. Sensharma, U. Garg, Q. B. Chen, S. Frauendorf, D. P. Burdette, J. L. Cozzi, K. B. Howard, S. Zhu, M. P. Carpenter, P. Copp, F. G. Kondev, T. Lauritsen, J. Li, D. Seweryniak, J. Wu, A. D. Ayangeakaa, D. J. Hartley, R. V. F. Janssens, A. M. Forney, W. B. Walters, S. S. Ghugre, and R. Palit, Phys. Rev. Lett. **124**, 052501 (2020).

[18] S. Nandi, G. Mukherjee, Q. B. Chen, S. Frauendorf, R. Banik, S. Bhattacharya, S. Dar, S. Bhattacharyya, C. Bhattacharya, S. Chatterjee, S. Das, S. Samanta, R. Raut, S. S. Ghugre, S. Rajbanshi, S. Ali, H. Pai, M. A. Asgar, S. Das Gupta, P. Chowdhury, and A. Goswami, Phys. Rev. Lett. **125**, 132501 (2020).

[19] J. Timár, Q. B. Chen, B. Kruzsicz, D. Sohler, I. Kuti, S. Q. Zhang, J. Meng, P. Joshi, R. Wadsworth, K. Starosta, A. Algora, P. Bednarczyk, D. Curien, Z. Dombrádi, G. Duchêne, A. Gizon, J. Gizon, D. G. Jenkins, T. Koike, A. Krasznahorkay, J. Molnár, B. M. Nyakó, E. S. Paul, G. Rainovski, J. N. Scheurer, A. J. Simons, C. Vaman, and L. Zolnai, Phys. Rev. Lett. **122**, 062501 (2019).

[20] S. Chakraborty, H. P. Sharma, S. S. Tiwary, C. Majumder, A. K. Gupta, P. Banerjee, S. Ganguly, S. Rai, Pragati, Mayank, S. Kumar, A. Kumar, R. Palit, S. S. Bhattacharjee, R. P. Singh, and S. Muralithar, Phys. Lett. B **811**, 135854 (2020).

[21] K. Rojeeta Devi, S. Kumar, N. Kumar, Neelam, F. S. Babra, M. S. R. Laskar, S. Biswas, S. Saha, P. Singh, S. Samanta, S. Das, S. Chakraborty, R. Singh, S. Muralithar, and A. Kumar, Phys. Lett. B **823**, 136756 (2021).

[22] C. M. Petrache, P. M. Walker, S. Guo, Q. B. Chen, S. Frauendorf, Y. X. Liu, R. A. Wyss, D. Mengoni, Y. H. Qiang, A. Astier, E. Dupont, R. Li, B. F. Lv, K. K. Zheng, D. Bazzacco, A. Boso, A. Goasduff, F. Recchia, D. Testov, F. Galtarossa, G. Jaworski, D. R. Napoli, S. Riccetto, M. Siciliano, J. J. Valiente-Dobon, M. L. Liu, X. H. Zhou, J. G. Wang, C. Andreoiu, F. H. Garcia, K. Ortner, K. Whitmore, T. Back, B. Cederwall, E. A. Lawrie, I. Kuti, D. Sohler, J. Timár, T. Marchlewski, J. Srebrny, and A. Tucholski, Phys. Lett. B **795**, 241 (2019).

[23] Q. B. Chen, S. Frauendorf, and C. M. Petrache, Phys. Rev. C **100**, 061301(R) (2019).

[24] Y. K. Wang, F. Q. Chen, and P. W. Zhao, Phys. Lett. B **802**, 135246 (2020).

[25] F.-Q. Chen and C. M. Petrache, Phys. Rev. C **103**, 064319 (2021).

[26] B. F. Lv, C. M. Petrache, R. Budaca, A. Astier, K. K. Zheng, P. Greenlees, H. Badran, T. Calverley, D. M. Cox, T. Grahn, J. Hilton, R. Julin, S. Juutinen, J. Konki, J. Pakarinen, P. Papadakis, J. Partanen, P. Rahkila, P. Ruotsalainen, M. Sandzelius, J. Saren, C. Scholey, J. Sorri, S. Stolze, J. Uusitalo, B. Cederwall, A. Ertoprak, H. Liu, S. Guo, J. G. Wang, H. J. Ong, X. H. Zhou, Z. Y. Sun, I. Kuti, J. Timár, A. Tucholski, J. Srebrny, and C. Andreoiu, Phys. Rev. C **105**, 034302 (2022).

[27] S. Frauendorf, Phys. Rev. C **97**, 069801 (2018).

[28] K. Tanabe and K. Sugawara-Tanabe, Phys. Rev. C **97**, 069802 (2018).

[29] E. A. Lawrie, O. Shirinda, and C. M. Petrache, Phys. Rev. C **101**, 034306 (2020).

[30] B. F. Lv, C. M. Petrache, E. A. Lawrie, A. Astier, E. Dupont, K. K. Zheng, P. Greenlees, H. Badran, T. Calverley, D. M. Cox, T. Grahn, J. Hilton, R. Julin, S. Juutinen, J. Konki, J. Pakarinen, P. Papadakis, J. Partanen, P. Rahkila, P. Ruotsalainen, M. Sandzelius, J. Saren, C. Scholey, J. Sorri, S. Stolze, J. Uusitalo, B. Cederwall, A. Ertoprak, H. Liu, S. Guo, J. G. Wang, H. J. Ong, X. H. Zhou, Z. Y. Sun, I. Kuti, J. Timár, A. Tucholski, J. Srebrny, and C. Andreoiu, Phys. Rev. C **103**, 044308 (2021).

[31] K. Tanabe and K. Sugawara-Tanabe, Phys. Rev. C **95**, 064315 (2017).

[32] B. F. Lv, C. M. Petrache, E. A. Lawrie, S. Guo, A. Astier, K. K. Zheng, H. J. Ong, J. G. Wang, X. H. Zhou, Z. Y. Sun, P. T. Greenlees, H. Badran, T. Calverley, D. M. Cox, T. Grahn, J. Hilton, R. Julin, S. Juutinen, J. Konki, J. Pakarinen, P. Papadakis, J. Partanen, P. Rahkila, P. Ruotsalainen, M. Sandzelius, J. Sarén, C. Scholey, J. Sorri, S. Stolze, J. Uusitalo, B. Cederwall, A. Ertoprak, H. Liu, I. Kuti, J. Timár, A. Tucholski, J. Srebrny, and C. Andreoiu, Phys. Lett. B **824**, 136840 (2022).

[33] S. Guo, X. H. Zhou, C. M. Petrache, E. A. Lawrie, S. H. Mthembu, Y. D. Fang, H. Y. Wu, H. L. Wang, H. Y. Meng, G. S. Li, Y. H. Qiang, J. G. Wang, M. L. Liu, Y. Zheng, B. Ding, W. Q. Zhang, A. Rohilla, K. R. Muhki, Y. Y. Yang, H. J. Ong, J. B. Ma, S. W. Xu, Z. Bai, H. L. Fan, J. F. Huang, J. H. Li, J. H. Xu, B. F. Lv, W. Hua, Z. G. Gan, and Y. H. Zhang, Phys. Lett. B **828**, 137010 (2022).

[34] K. Nomura and C. M. Petrache, Phys. Rev. C **105**, 024320 (2022).

[35] W. X. Shi and Q. B. Chen, Chin. Phys. C **39**, 054105 (2015).

[36] B. Qi, H. Zhang, S. Y. Wang, and Q. B. Chen, J. Phys. G: Nucl. Part. Phys. **48**, 055102 (2021).

[37] I. Hamamoto, Phys. Rev. C **65**, 044305 (2002).

[38] I. Hamamoto and B. R. Mottelson, Phys. Rev. C **68**, 034312 (2003).

[39] Q. B. Chen, S. Frauendorf, N. Kaiser, U.-G. Meißner, and J. Meng, Phys. Lett. B **807**, 135596 (2020).

[40] C. Broocks, Q. B. Chen, N. Kaiser, and U.-G. Meißner, Eur. Phys. J. A **57**, 161 (2021).
[41] L. Hu, J. Peng, and Q. B. Chen, Phys. Rev. C **104**, 064325 (2021).
[42] H. Zhang, B. Qi, X. D. Wang, H. Jia, and S. Y. Wang, Phys. Rev. C **105**, 034339 (2022).
[43] H. M. Dai, Q. B. Chen, and X.-R. Zhou, Phys. Rev. C **108**, 054306 (2023).
[44] A. A. Raduta, R. Poenaru, and L. G. Ixaru, Phys. Rev. C **96**, 054320 (2017).
[45] A. A. Raduta, C. M. Raduta, and R. Poenaru, J. Phys. G: Nucl. Part. Phys. **48**, 015106 (2021).
[46] C. M. Raduta, A. A. Raduta, R. Poenaru, and A. H. Raduta, J. Phys. G: Nucl. Part. Phys. **49**, 025105 (2022).
[47] R. Budaca, Phys. Rev. C **97**, 024302 (2018).
[48] R. Budaca, Phys. Rev. C **103**, 044312 (2021).
[49] R. Budaca and C. M. Petrache, Phys. Rev. C **106**, 014313 (2022).
[50] Y. R. Shimizu and M. Matsuzaki, Nucl. Phys. A **588**, 559 (1995).
[51] M. Matsuzaki, Y. R. Shimizu, and K. Matsuyanagi, Phys. Rev. C **65**, 041303(R) (2002).
[52] M. Matsuzaki and S. I. Ohtsubo, Phys. Rev. C **69**, 064317 (2004).
[53] M. Matsuzaki, Y. R. Shimizu, and K. Matsuyanagi, Phys. Rev. C **69**, 034325 (2004).
[54] Y. R. Shimizu, T. Shoji, and M. Matsuzaki, Phys. Rev. C **77**, 024319 (2008).
[55] T. Shoji and Y. R. Shimizu, Prog. Theor. Phys. **121**, 319 (2009).
[56] S. Frauendorf and F. Dönau, Phys. Rev. C **92**, 064306 (2015).
[57] M. Shimada, Y. Fujioka, S. Tagami, and Y. R. Shimizu, Phys. Rev. C **97**, 024318 (2018).
[58] Q. B. Chen, S. Q. Zhang, P. W. Zhao, and J. Meng, Phys. Rev. C **90**, 044306 (2014).
[59] Q. B. Chen, S. Q. Zhang, and J. Meng, Phys. Rev. C **94**, 054308 (2016).
[60] Q. B. Chen, S. Q. Zhang, P. W. Zhao, R. V. Jolos, and J. Meng, Phys. Rev. C **87**, 024314 (2013).
[61] Q. B. Chen, S. Q. Zhang, P. W. Zhao, R. V. Jolos, and J. Meng, Phys. Rev. C **94**, 044301 (2016).
[62] X. H. Wu, Q. B. Chen, P. W. Zhao, S. Q. Zhang, and J. Meng, Phys. Rev. C **98**, 064302 (2018).
[63] M. Kitagawa and M. Ueda, Phys. Rev. A **47**, 5138 (1993).
[64] J. Klauder and B. Skagerstam, *Coherent States: Applications in Physics and Mathematical Physics* (World Scientific, Singapore, 1985).
[65] D. Janssen and I. Mikhailov, Nucl. Phys. A **318**, 390 (1979).
[66] S. Frauendorf, Phys. Scr. **93**, 043003 (2018).
[67] B. Podolsky, Phys. Rev. **32**, 812 (1928).
[68] W. Pauli, in *Handbuch der Physik* (Springer-Verlag, Berlin, 1933), Vol. XXIV, p. 120.
[69] S. Frauendorf, Nucl. Phys. A **557**, 259 (1993).
[70] S. Frauendorf, Nucl. Phys. A **677**, 115 (2000).
[71] J. D. Lewis, T. B. Malloy, Jr., T. H. Chao, and J. Laane, J. Mol. Struct. **12**, 427 (1972).